MAPPING OF GLACIER EXTENT USING DEEP LEARNING METHOD

PRASHANT
ENSCHEDE, the Netherlands, June 2022

Thesis submitted to the Faculty of Geo-Information Science and Earth Observation of the University of Twente in partial fulfillment of the requirments for the degree of Master of Spatial Engineering

Supervisors:
Dr. Claudio Persello
Dr. Hossein Aghababaei

Scientific Advisor
Dr. Thomas Schellenberger, University of Oslo

Thesis Assessment Board
Prof. dr. ir. A. Stein (Chair)

Dr Carlo Marin (External Examiner, EURAC Research Institute, Bolzano, Italy)

FACULTY OF GEO-INFORMATION SCIENCE AND EARTH OBSERVATION
UNIVERSITY OF TWENTE, ENSCHEDE, THE NETHERLANDS

Abstract

Glaciers are extremely sensitive to changing climatic conditions. Thus, they are among the 54 Essential Climate Variables (ECV) identified by the Global Climate Observation System (GCOS). The catastrophic consequences of the continuous rise in temperature are glacial retreat and loss of glacial mass, leading to sea-level rise, fresh water loss, hydrological shift, habitat loss, etc. Glaciers from the Arctic, Antarctic, Himalayas, or Alps are continuously receding. It is essential to monitor glacier parameters such as length, mass, area, and extent. This research aimed to map the glacier extents of Jostedalsbreen and Svalbard, Norway using open-source Sentinel-1 and Sentinel-2 satellite data using a novel deep learning-based data fusion method. We investigated the sequence of band combinations of SAR and optical data in pre-designed fully convolutional networks, FCNDK-6, SegNet, UNet, and ResUnet, to delineate accurate glacier extents.

In Sentinel-1 experiments, our 3-band experiments provided a comparatively higher F1 score, but at the same time, SegNet has almost 20% less accurate prediction value than the UNet model. After multiple trials of the model, we observed that, in the case of Sentinel-1 VV and VH polarization data, FCNDK and the UNet have stable output. However, the accuracy from the UNet was more consistent, delivering a higher F1 score. Sentinel-2-based model performance was higher than the Sentinel-1-based model. We ran all networks in two different input setups (spectral band combinations); first, we used Blue, Green, Red, and Near Infrared (NIR) bands and achieved an F1 score of 0.88. Later we included shortwave infrared (SWIR) and other NIR bands and used twelve bands as input. In the 12-band experiment, we observed that the same UNet model (used for the 4-band experiment) increased the accuracy by 2% and managed to have an F1 value of 0.90. In our novel experiment, we fused the Sentinel-1 and Sentinel-2 datasets and checked their influence on the resultant mapping of glacier extents. We realized that fusing the data from these two optical and SAR satellites improved the F1 value. We also observed that the same model with a standalone method gave better results with fusion data. For example, FCNDK with Sentinel-1 3-band experiment has an F1 score of 0.73, and Sentinel-2 4-band experiment has 0.83, and when we fused the same three-channel derived from VV and VH polarization of S1 and four bands from S2 and performed a 7-band fusion experiment, we achieved 0.88 of F1 score. Our final attempt experiment concluded that the 18-band fusion experiments provided the best result. This research concluded that UNet is a robust model for accurate glacier extent mapping and can contribute to building and updating glacier databases.

Keywords: Deep learning, Sentinel-1, Sentinel-2, Glacier mapping, Fusion

Acknowledgment

I would start this section with my special gratitude and give credit for guidance to my supervisor, dr. Claudio Persello, for his continuous support and guidance, has been essential to this work. I very much enjoyed our discussion session, and much appreciated the freedom of space to work independently. While on the other hand, I want to thank my other supervisor, dr. Hossein Aghababaei who has always directed my thoughts toward a higher dimension.

Furthermore, I am very grateful to dr. Thomas Schellenberger, he has always been supporting me and made sure that I have all the quality data for my research. It was unfortunate that we never had a chance to meet physically during the research, but his online meeting helped me learn more about the glaciers.

In practical life, sometimes things are incomplete or impossible in the absence of money, which was also a reason for me to continue studying. So I am very grateful for providing me with the financial support as a scholarship and for selecting me for the ITC fellowship for spatial engineering.

I am also very much appreciative of the administration of the Faculty ITC, especially drs. Tiny Luiten, Marie Chantal, Thereza Boogaard, and Jorike Siemerink for their continuous support. I would also express my sincere gratitude to all professors and faculties who taught me during this study and helped me to expand my knowledge.

I got special attention during this research while writing the codes or understanding the different models. It would not be possible without experts' help, especially Anirudha, Bedru, Konstantin, Sagar, Srikumar, and Hillary. Special thanks to these beautiful minds. I am also very thankful to dr. Serkan Girgin, including his ITC-CRIB platform, allowed me to run my models smoothly. So huge thanks to the CRIB team.

As I know a miserable personality, when it comes to mentioning the name of my closest people, I am again being miserable and intentionally do not mention their names, but I am very grateful for their emotional support. I can say you guys never let me have a feeling of loneliness and boosted my energy while visiting my house, inviting me for dinner, sharing a laugh at the lunch table, playing cards during the evening snacks, and asking about my wellness in the cafeteria, or taking me out for a walk.

Lastly, I want to thank my family and friends back home; they have been a strong backbone of support throughout the years. Finally, the artist Bregje who has constantly been sending me positive energy and joy while summing up my writings.

Table of Contents

List of figures

List of tables

1 INTRODUCTION

Glaciers are one among 54 Essential Climate Variables (ECV) identified by the Global Climate Observation System (GCOS) as they respond sensitively to climate change (Rabatel et al., 2017a; WMO et al., 2011). Glaciers are the major freshwater source for living creatures (Wang et al., 2021). Humans and animals (Jacobsen et al., 2012) are highly affected due to changes in glacial areas (Gupta et al., 2005), as it is a major source of freshwater. Additionally, glaciers play an essential role in the local and global hydrological monitoring system(Hollmann et al., 2013). Continuous changes in climate patterns, reduction of freshwater (Gore et al., 2019), rise in sea level (Huss and Hock, 2015), and glacial hazards (Bolch et al., 2011) are significant threats to different lifeforms on earth (Jacobsen et al., 2012). Therefore, it is vital to have information about the glaciers and their features.

Remote sensing-based techniques offer the opportunity for seamless monitoring of glaciated areas. Remote observations offer the capacity to perform regional and minute mapping while modeling glacial processes. One such approach utilizes the correlation between glacier surface states (snow cover, glacier facies, albedo) and glacier surface mass balance (excluding frontal ablation rates) (Rabatel et al., 2017b). Glacier areas, combined zones of accumulation, and ablation have different surface characteristics. The ablation zone meets with different landforms of non-glacier features, likely creating a contour around the glaciers, called the glacier boundary (F. Paul et al., 2013). This glacier boundary separates the glacier and non-glacier areas. Glacier facies are generally various surface properties stretching from fresh ice or snow-covered ice in the accumulation region to gradually more extensive and progressively deeper debris cover from the equilibrium line altitude to the Glacier (Bolch et al., 2008; Kundu and Chakraborty, 2015; Pope, 2013; Xie et al., 2020). In addition, some glaciers may be encircled by periglacial deposits, sediments, lateral moraines, end moraine, and supra glaciers (Bishop et al., 2000; Echelmeyer et al., 1992; Gupta et al., 2005).

The present methods for mapping glacier boundaries, facies, and generating data inventories prominently utilize visual identification of target features using scene knowledge (Barzycka et al., 2020; Shukla and Ali, 2016), followed by information extraction methods such as band-rationing and image classification (both unsupervised and supervised) (Pope and Rees, 2014a). Normalized difference indices are extremely useful when trying to segregate features in multispectral imagery. A popular index called normalized snow index (NDSI) is extensively and efficiently used to separate the glacier and non-glacier areas (Pope and Rees, 2014b). Also, the existing techniques can map glacier extent or calving front, glacier facies like dry and wet snow, snow line (an estimation of the equilibrium line altitude (ELA)), ice, firn, and the evolution of the firn area (Xie et al., 2020). However, despite continuous progress in the extraction methodology, most are manual, complicated, and time-consuming while processed within a large study area (Sibandze et al., 2014).

Continuous development of machine learning techniques supports the researchers in analyzing extensive spatial data and extracting the fine features for better understanding. Deep learning methods, such as neural networks, utilize several processing layers to detect structure and patterns in enormous data sets(Rusk, 2016). Convolution neural networks (CNNs) are deep architectures containing convolutional, non-linearity, pooling, and fully connected layers (Albawi et al., 2017). CNN performed outstanding while classifying the image data and achieved remarkable results (Albawi et al., 2017).

Fully convolution networks (FCNs) have emerged in recent times. They are widespread after the availability of big data and the development of computational hardware such as Graphical Processing Units (GPUs). They are an extensively used technique in image analysis, feature extraction, and image segmentation (Zhong et al., 2016). The deep learning approach of the FCN uses the image segmentation method, where each pixel of the image is assigned a label as one specific class. This approach helps identify the object through simple image classification and locate the object's boundaries, which helps to have a more accurate understanding of the object. This technique is emerging in earth observation because of its reduced processing time and higher result accuracy than the traditional method. This method uses pixel-based analysis and assigns a label to every satellite image pixel. The architecture learns the key features from the raw data using a feature extractor. It gets down-sampled while passing through the convolution layer. The fully connected layers of these traditional CNN models are used for classification in object detection tasks. The image segmentation models won't reuse those fully connected layers achieved in FCN. In most glacier research, shallow machine learning methods have been applied, and there is a huge opportunity with FCN. This research is focused on mapping the glacier extent with open-source Sentinel-1 and Sentinel-2 data using the fully convolutional deep learning approach.

1.1 State of Art

Information about the glacier's extent and its surface features help to estimate the changes in the mass of the Glacier (Cogley et al., 2010). Accurate and detailed glacier boundary extraction is fundamental for any glacier research. According to the research (Paul and Kääb, 2005), several climate models require an accurate baseline inventory of the glacier to study climate change. The ongoing climate crisis, continuous increase in temperature, and high melt of the Arctic, Antarctic, Alps, and the Himalayas, increase the demand to have the updated glacier boundary for these regions. The high spatial and temporal resolution data is urgent to monitor the small changes in these regions, such as the glacier facies and glacier extend, which also plays a vital role in understanding the glacier energy balance (Bhardwaj et al., 2015).

Fieldwork is an integral (Hubbard and Glasser, 2005) and crucial (Negrel et al., 2018) component of glaciology. Extensive and expensive logistics, hostile weather, and intensive landscapes (Bhardwaj et al., 2016) result in challenges for data collection from every part of the glacier. Nevertheless, it is necessary to have field data to calibrate any remotely collected data (Andreassen et al., 2002). The complexity of field data collection and the high cost of very high-resolution spatial data verifying remotely collected data increase the problems.

Remote sensing tools provide an extensive alternative to produce data solutions for data production at different spatial, spectral, and temporal resolutions for inaccessible glaciers (Shukla and Yousuf, 2017). Advances in remote sensing techniques opened the door to understanding the process and paved the way for continuous mapping and monitoring of glacier facies and their extent (Brown, 2012; de Angelis et al., 2007; Pope, 2013). Data collected on different spectral wavelengths allow to do various glacial analyses. The unique responses of glacier properties in different wavelength ranges permit a wide range of mapping techniques (Gupta et al., 2005; Singh et al., 2010), i.e., for example, optical data allows having enables a visual surface analysis (Racoviteanu and Williams, 2012; Shimamura et al., 2006), whereas synthetic aperture radar (SAR) data help to do the permits subsurface analysis of glacier regions (Winsvold et al., 2018). For example, fresh snow with its physical properties can be easily interpreted in optical data(Heiskanen et al., 1993; Yousuf et al., 2019), whereas the backscattered value of radar helps to identify dry and wet snow as it reduces the backscattered intensity due to increased water content (Pellikka and Rees, 2009; Rau et al., 2000; Tran et al., 2008).

Spectral reflectance data collected from multispectral remote sensing satellites attracts glaciologists to perform analysis for various applications, such as facies classification (Shridhar Digambar Jawak et al., 2019), Glacial, and non-glacial area mapping (Paul and Kääb, 2005; Pope and Rees, 2014a; Yavaşli et al., 2015), albedo measurement (König et al., 2001; Pope and Rees, 2014b), glacial extent mapping (Yavaşli et al., 2015), etc. Normalized difference snow index (NDSI) (Riggs et al., 1994)use the ratio method to differentiate snow and non-snow area by using the spectral information of the green band and short-wave infra-red band (Kulkarni et al., 2002). The snow has high reflective properties in the visible spectral band whereas high absorption characteristics in short wave infra-red, which allows these two spectral bands to measure the comparative magnitude of the reflectance (Hall and Riggs, 2010). Apart from these benefits, multispectral satellite images have limitations due to clouds (Hall et al., 1995). Researchers use radar remote sensing data to overcome this limitation of optical satellite imaging(Shi and Dozier, 1993).

Radar remote sensing works in the microwave range, allowing it to penetrate through clouds, which helps identify more glacier features. Radar measures the backscatter instead of radiance, which allows to collect the information down to the upper surface. Therefore, the glacier information depends on the surface roughness and dielectric properties (Pellikka and Rees, 2009). Synthetic-aperture radar (SAR) data successfully mapped wet and dry snow (Joshi et al., 1998), classified surface facies, and identified the snowline using quad polarization data (Huang et al., 2011). The classification of glacier area depends on the volume scattering of the snow and the surface scattering of the snow-air interface (Jiancheng Shi and Dozier, 1995).

Combining optical and radar imagery can identify the features of the upper surface and down it simultaneously (Pope, 2013). Data fusion from SAR and optical sensors allows precise interpretation and analysis by providing the insights information. Combining data from SAR with multispectral bands can help identify features like firn and superimposed ice as both have similar characteristics (Pope, 2013), Glacier and sea ice. Likewise, the data fusion can classify and map the clean glacier and melt surfaces(Brown, 2003).

1.2 The wicked problem and glacier

Stocke (2014) mentioned the catastrophic outcomes of the continuous rising temperature toward the fast melting of glaciers and ice sheets. This leads to complex, alarming consequences, such as sea-level rise, fresh water loss, hydrological shift, habitat loss, etc. Pachauri et al. (2014) referred to glaciers as the most sensitive indicator of climate change. Glaciers form where climatic conditions and topographic conditions permit snow to accumulate, which leads to the decadal and slow process of transforming snow into glaciers (Stocker, 2014). The flow of glaciers always depends on the elevation, topography, and temperature. Lower elevations near the glacier tongue are dominated by ablation. Combining accumulation and ablation helps to determine the mass balance. Continuous surface melting corresponds to the uninterrupted ablation and heavy ice loss. Constant loss of energy parallel to the runoff connects surface mass losses and is interlinked to atmospheric conditions (Pörtner et al., 2019). This can be monitored over time to link to the changing planetary temperature.

At the same time, continuous glacier melting is a big threat to our planet and its species. Glaciers from the Arctic, Antarctic, Himalayas, or Alps are retreating day by day, making it important to monitor the glacier parameter, such as length, mass, area, etc. In-situ measurements of the glaciers include many challenges such as accessibility to the glacier location, disaster risk, installation of the equipment, etc. Earth observation with remote sensing techniques such as satellite imaging and aerial photography are influential in overcoming this situation. The global glacier database such as Global Land Ice Measurements from Space (GLIMS) (Raup et al., 2007) and Randolph Glacier Inventory (RGI) (Pfeffer et al., 2014) are meant to resourceful. The alarming climate change scenario now made it more needful and demanding to precisely update these databases to a great temporal and spatial extent. The proper and precise update of the glacier database is still a challenge with remote sensing imaging, such as the availability of cloud-free optical satellite images, improper methods, big geo-data handling etc. (Nijhawan et al., 2019).

Table 1.1: Wickedness effect on the different stakeholders

	Actors	**Effects**	**Influence**
Local	Biodiversity	- Species are endanger - Habitat loss	- Changes in runoff magnitude and seasonality
	Local population	- effects their fresh water source - flash flood danger due to outburst floods	- health, and diseases - disaster
	Local government	- Monitoring and Management - Economy	
	Local tourism	- Decrease - Demand loss	
Global	Industry	- Hydro plants (Energy companies) - Fishing problem - Insurance loss	- hydrological infrastructure

	Weather and Climate	- The melting of the glacier makes a huge difference in local, and global temperature	

1.3 Research gap and problem statement

While deep learning techniques have been effectively applied for mapping glacier features (i.e., mapping the glacier extent), the architecture used for mapping various glaciers has not been consistent. The problem mentioned in section 1.2, such as the availability of cloud-free image, unstable method for glacier area mapping, and the big geo-data handling, needs to be addressed. To overcome this cloudy images problem, Dirscherl et al. (2021) applied optical and SAR datasets and tried to fill the datasets gap while the research such as (Alifu et al., 2020; Khan et al., 2020; Xin et al., 2018; Zhang et al., 2019) contributing the overcome the problem of influential method, and big-geodata handling.

Xie et al. (2020) stated further development in their CNN architecture while considering spatial constraints, surface morphologies, and flow geometries. These considerations will help modify the CNN architecture according to the complexity of glacier dynamics (tectonic forcing, internal deformation, basal sliding, basal motion, Anisotropy, hydrostatic pressure, normal stress, shear stress, bed deformation, etc.) as well as geographical variation.

This research is also trying to achieve and contribute to the United Nations (UN) Sustainable Development Goals (SDGs) for climate action by helping to have proper and regular glacier monitoring. As aforementioned, it is important to have access to accurate knowledge about the glacier extent. We are trying to achieve this goal by achieving a robust method for glacier mapping, which can overcome the problem of three major problems (accurate model, big-geodata handling, and cloudy images) during the use of remote sensing for glacier studies.

1.4 Research identification

There is numerous research, but the proper and efficient method is still a question. The majority of the existing methods are shallow machine learning, while accurate glacier extent mapping is still challenging, which leads to the scope of improvement. This research addresses the problem of glacier area mapping with the help of deep learning networks, where we are investigating data from different satellite sensors such as optical and SAR data. We used four different pre-developed networks: Fully convolution neural Networks with kernel dilution (FCN DK), SegNet, UNet, and the ResUnet. Additionally, this research tries to fulfill the data and method gaps by utilizing optical, SAR, and fusion of optical and SAR data. We also consider promoting open science and using open-source satellite data and open codes during this research.

1.5 Research Objectives

With the unprecedented changes in glacial systems and the ongoing climate change, there is a need for up-to-date information on essential glacial dynamics. This can be accomplished by achieving the objective and sub-objective.

1.5.1 Main Objective

The main objective of this research is to map the glacier extent using optical and synthetic aperture radar images.

1.5.2 Sub-Objectives

The following sub-objectives are addressed to achieve the main objectives:

1. To extract and map the glacier extent using Sentinel-1 and Sentinel-2 images.
2. To explore the possibility of data fusion (Sentinel-1 and Sentinel-2) for glacier extent mapping.

1.6 Research Questions

The research question mentioned below is formulated to facilitate achieving the objectives and sub-objectives. Some questions are specific to the individual objectives, whereas some of it is addressing both.

Specific to sub-objective 1

1. What is the overall accuracy that can be achieved when separating glacier and non-glacier extent using standalone Sentinel-1 and Sentinel-2 imageries?

Specific to sub-objective 2

2. What is the overall accuracy that can be achieved after fusing Optical and SAR data to map the glacier extent?
3. Which band combinations of Sentinel-1 and Sentinel-2 efficiently improve the glacier area mapping?

Applicable to sub-objective-1 and sub-objective-2

4. How can the different combinations of SAR data help to map glacier extent?

1.7 Research innovation

The novelties in this research are as follows:

- To improvise methods specific to the glacier boundary delineation
    - The deep learning network use multi-sensor, Sentinel-1, and sentinel-2 data, which is fused out of the network.
- Investigate the combination of hyperparameters for the networks to specify glacier and non-glacier areas precisely
- Implementation of segmentation network of glacier area mapping.

2 LITERATURE REVIEW

2.1 Glacier extent mapping

The extent of the glacier is derived from its area cover, which separates glacier or snow/ice-covered areas from non-glacier areas, and is also termed the glacier outline (Paul et al., 2013). Glacier facies highlight the physical characteristics of variation in snow and ice(Benson, 2001). Glacier facies (Figure 2.1) are also termed as the glacier zone (Benson, 1959; Müller, 1962; R. S. Williams et al., 1991). The concept of the glacier facies is essential when analyzing the different types of ice and snow (Richard S Williams et al., 1991), including their variations in altitude and seasons (Benson, 1959; Paterson, 1994).

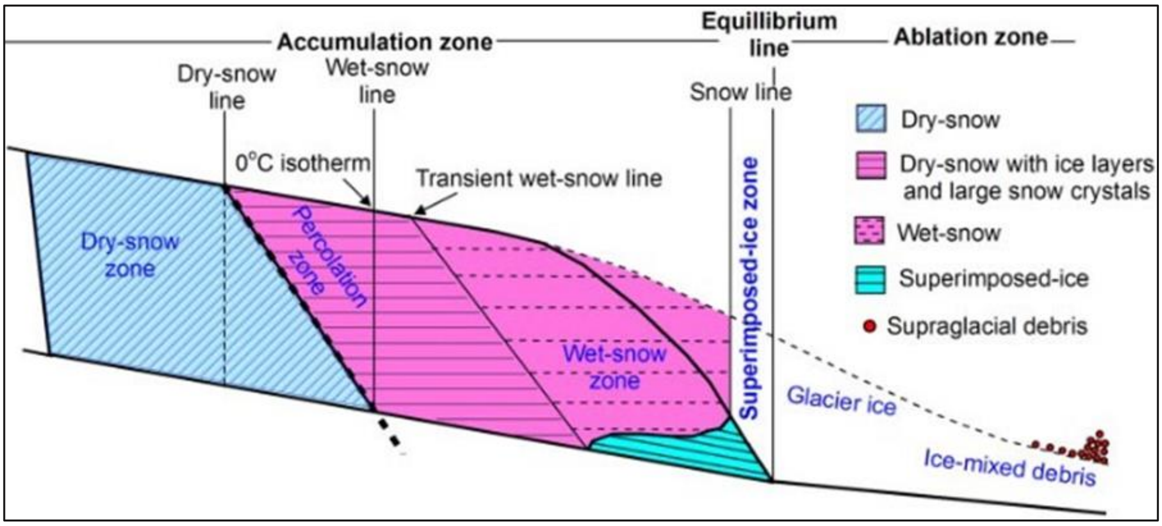

Figure 2.1 : Division of glacier facies on its surface(Image Source: (Yousuf et al., 2019)

Glacier extent can be detected and classified using satellite remote sensing techniques. Østrem, (1975) successfully demonstrated the relationship of multi-year ground data from Norwegian glaciers' equilibrium-line altitude with the Landsat MSS satellite. Later, Williams, (1987) processed Landsat MSS and Landsat 5 TM data to map 8300 km² of the ice cap and delineated the firn line on the Vatnajokull glacier in Iceland. Development in satellite sensors allows continuous updates with extraction and mapping methodology to achieve the highest accuracy (R. S. Williams et al., 1991).

Literature reveals that remote sensing data for snow and ice mapping is growing day by day. It also allows for regular updates in the methodology of satellite data processing. Literature has further revealed that one feature extraction method has not always fitted to map multiple glaciers. In the past, that methodology has changed with different glaciers and remote sensing data (Pope and Rees, 2014b). The combination of the multispectral band helped enhance the glacial features (Bhardwaj et al., 2015; König et al., 2001). The band ratio method has effectively separated the accumulation and ablation zone (Jawak et al., 2019). They considered the spectral signature of different bands of satellite images further classify the snow and ice features from the accumulation and ablation zone (Nolin and Payne, 2007). Later the development of synthetic aperture radar sensors effectively influenced the study of glacier regions. These active sensor technologies minimize the dependence on the weather (Partington, 1998).

2.2 Glacier mapping using remote sensing data

Mapping glacier extent with image analysis techniques is often performed using image segmentation (Mohajerani et al., 2019). In contrast, glacier mapping has higher accuracy with supervised methods (Jawak et al., 2019). Some customized semi-automated protocols using supervised image analysis techniques successfully extract snow, ice, mixed debris, and debris. These semi-automated methods mainly classify the glacier using spectral band rationing, object-based, and pixel-based classification approaches (Jawak et al., 2019). An automatic approach for mapping glacier extent and glacial surface features is challenging. Still, machine learning (ML) has been effectively used to map glaciers in recent development (Mohajerani et al., 2021)using approaches such as K-nearest neighbors (KNN) (Alifu et al., 2020), Support vector machine (SVM) (Huang et al., 2011), Multi-layer perceptron (MLP) (Alifu et al., 2020), Random forest (RF) (Khan et al., 2020; Wang et al., 2021; Zhang et al., 2018), Decision tree (DT) (Albright et al., 1998; Racoviteanu and Williams, 2012), artificial Neural network (ANN) (Khan et al., 2020). Wang et al., (2021) managed to monitor the total glacier area and successfully classified the glacial and non-glacial features using the RF techniques. Extraction of ice shelf front in Antarctica using Sentinel-1 satellite data was demonstrated using the CNNs where (Baumhoer et al., 2019) trained the neural network for the Antarctic region with the massive amount of Sentinel-1 dataset to generate the information about the Antarctic coastline. The commercial satellite's high level of spatial resolution (e.g., World View, QuickBird, etc.) also allowed mapping glacier extent, significantly improving glacier studies; high-resolution satellite data helps train models for accurate results (Yavaşli et al., 2015). The accuracy of the methods used to extract glaciers is essential due to several cryospheric findings, and economic improvements rely on it. Hartmann et al., (2021) mapped the calving front but mélange with features mixed with icebergs and sea ice since these surface features are somewhat similar in properties and texture. Some features developed in melting areas of glaciers like supra glacier lakes are successfully delineated with uncertainties of glacial streams, ice crevasses, and water channel stripes (Chen, 2021).

In recent glacial studies, deep learning methods have also approached and efficiently mapped snow and glaciers. Nijhawan et al., (2019) applied a deep learning approach to map snow and non-snow area using Sentinel-1/2 images. In the first step, the researcher used the Sentinel-2 image to extract features using AlexNet, and the feature reduction was achieved using principal component analysis (PCA). The extracted features were further fed into the RF classifier. In the second step, the researcher used VV and VH polarization images of Sentinel-1 along with DEM-derived parameters (surface curvature, slope, and aspect) to produce the result using another RF classifier. The researcher used collective classification results to make the final snow and non-snow classification in the final step. In another study, (Xie et al., (2020)proposed a deep learning approach named GacierNet to map the boundary of a debris-covered glacier in the Himalayan and Karakoram range of glaciers using Landsat-8 data. The GlacierNet CNN is a SegNet-based architecture that includes encoding and decoding as two main processes designed to consider the spatial characteristics (texture, patterns, variation, and Anisotropy).

2.3 Deep learning

Deep learning (DL) is the subset of machine learning and is derived from the field of Artificial Intelligence (AI) (Patterson, and Gibson, 2017). From a broad perspective, AI is an umbrella for all techniques which enable the computer to act intelligently. Machine learning allows computers to modify or adapt their actions and predictions with the help of the learning process (Marsland, 2011). Deep learning can be defined as a "neural network with a substantial number of layers and parameters" (Patterson, and Gibson, 2017). In deep learning, the algorithm is designed in such a way that the machine also learns the features from the data.

Compared to shallow machine learning, deep learning approaches are more efficient with high-dimensional data, which helps interpret in different ways, such as texts, sounds, and images (Xin et al., 2018; Zhang et al., 2018). Deep learning uses the machine learning method of data learning but has several hidden layers. In deep learning techniques, a single image can be expressed in numerous ways, for example, pixel intensity, shape, region, edges, and so on (Xin et al., 2018). These all-physical characteristics further help the deep learning architecture to learn tasks easily. Among the advantages of DL is its fast-learning approach. The non-linear processing approach in multiple layers allows the layers to take the output result of the previous layer as their input, which helps with the accuracy and performance of the system (Dargan et al., 2020).

Recent development in deep learning helped the researcher extract features from images, either classifying or segmenting them. A Fully convolution Network (FCN) works with the concept of CNN, and the FCN works with a layer as a deep filter while computing the general non-linear function (Long et al., 2015). Fully convolution network can operate with the input of any size and delivers an output of equivalent spatial dimensions. The number of layers in FCN varies with variation in architecture, but most of them consist of the input layer, convolutional layer, activation, pooling, upsampling, classification, and output layer. These layers of the network perform their task in a pre-defined manner. The convolution layer is important in architecture. These layers convolute input and help learn its feature using the learnable filters. These filters are dimensionally defined in the form of $f\ x\ c\ x\ k$, where f is the kernel size of the filter, c indicates the total number of input bands, and k represents the total number of filters which helps to recognize the patterns in the image. Another important layer is batch normalization, which helps with the processing speed by adjusting/reducing the covariate shift. Another layer, along with the convolution and batch normalization layers, is non-linearity. In networks, non-linear layers vary, such as rectified non-linear units, TanH, or the sigmoid. In image classification, ReLu is largely used non-linear layers because of its robustness. Later on, the pooling layer after these three layers, which is used to decrease the spatial dimensionality, there are different types of pooling layers such as max-pooling, average-pooling, etc. Some of the most used examples of FCN are SegNet (Xie et al., 2020), and UNet (Baumhoer et al., 2019; Chen, 2021; Dirscherl et al., 2021; Hartmann et al., 2021; Holzmann et al., 2021). These techniques are utilized effectively to resolve multiple complex tasks while applying in image processing with exceptional accuracies.

2.4 Sentinel-1, and Sentinel-2 image fusion

The recent development of the data accessibility and availability of a similar mission provided the opportunity to combine data from two or more sensors. Sentinel-1 (S-1) and sentinel-2 (S-2) products complement each other while exploring the relevant information in multiple domains, such as marine, atmosphere, climate change monitoring, etc.Fernandez-Beltran et al., (2018) and Yokoya et al., (2017) applied and successfully fused the multispectral and SAR image at three different levels, pixel, feature, and the decision level, and explained that combining the bands from different sensors as the most relevant method.

Sentinel-1, the C-band-based sensor of the European space agency, uses more than one polarization to emit and receives the signals. These polarization features of the S-1 allow extraction of ample information from the observed earth's features. When it comes to processing the polarimetric SAR, the classification is generally based on the covariance or coherency matrix. The output of these matrices is future processed with speckle filtering and later the feature extraction or classification(LEE et al., 1994). In some researchers, such as Liu et al., (2016) and Mullissa et al., (2017), applied scattering properties derived using the polarimetric decomposition to highlight and extract the feature. Cloude and Pottier (1997) proposed methods that allow to extraction three-component (called Entropy, Anisotropy, and Alpha) based on the scattering mechanism of different polarization. The properties of Entropy, Anisotropy, and Alpha vary with the change in scattering properties, relays on the surface roughness, and are influenced by speckles.

3 STUDY AREA

3.1 Jostedalsbreen

Jostedalsbreen is one of the largest glaciers in Europe (Figure *3.1*). It is located in the Vestland county in western Norway and extends into four municipalities (Luster, Sogndal, Sunnfjord, and Stryn). The total area extent of this Jostedalsbreen is 474km^2, which includes almost fifty small and big glaciers. Some of the well-known glaciers are Boyabreen, Nigardsbreen, Briksdalsbreen, and Lodalsbreen, etc. These small glaciers are of different types, such as outlet glaciers and regenerated glaciers. There has been a continuous loss of mass since 1984; the total area of Jostedals has been reduced by 9% since 1966 (Andreassen et al., 2012). Saetrang and Wold (1986) revealed that the ice thickness of the Jostedalsbreen is up to nearly 600m, where most of the area varies between 150m and 300m. Being a part of the Scandinavian Mountains range, the glacier area has a variation of about 1500 m in its minimum and maximum elevation from the ground level (Laute and Beylich, 2021). An increase in temperature in this area leads to a rise in the number of glacial lakes (Laute and Beylich, 2020).

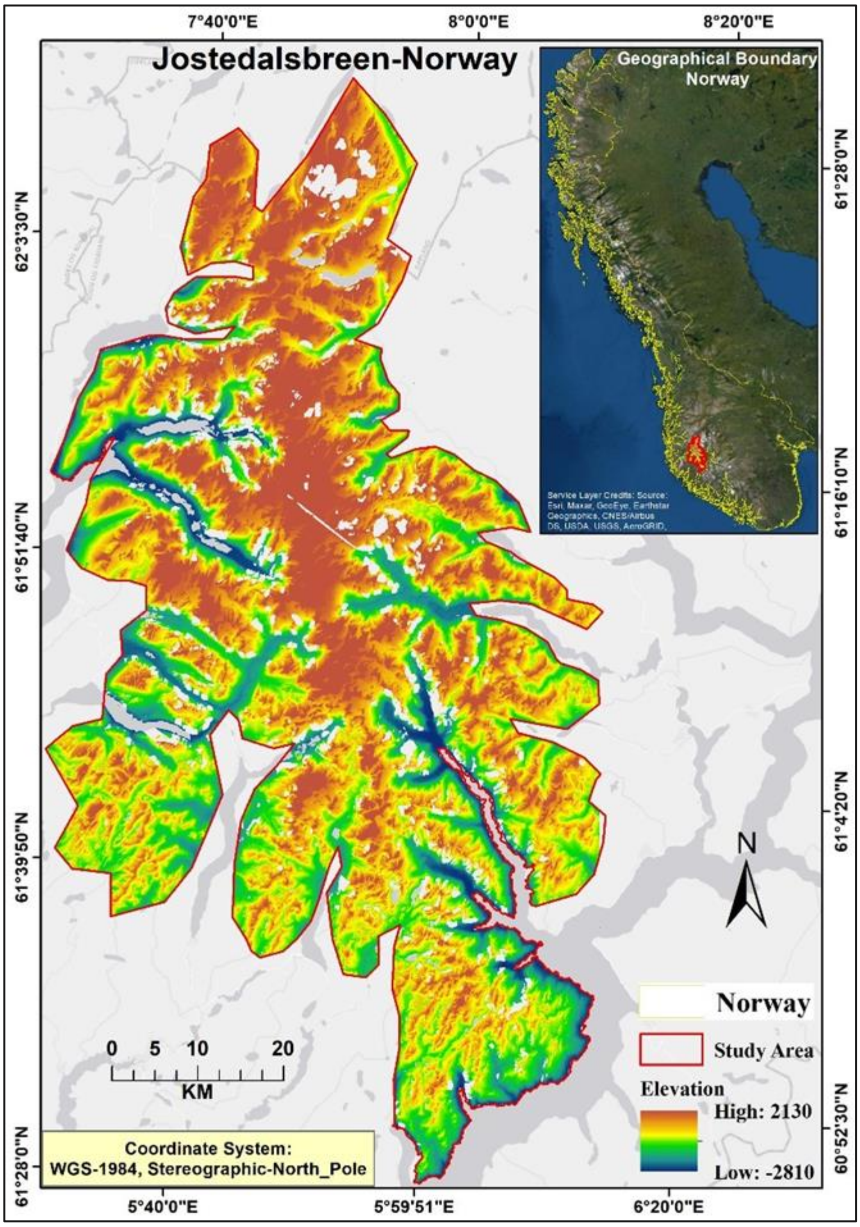

Figure 3.1 Study area site-1 Jostedalsbreen, Norway

3.2 Svalbard

Svalbard is an island in the Arctic Ocean (Figure 3.2). It is a part of the Norwegian kingdom, but it is not a part of its geographical boundary (Arlov, 2006). The Svalbard treaty signed in 1920 has special jurisdiction, allowing Norway to have administrative supervision (Arlov, 2006). It is the northernmost human living territory and lies in the Arctic circle. Svalbard experiences 24hrs of the night during the winter and 24hours of the sun during the summer (Nuth et al., 2013). Geographically, the 60% area of Svalbard is covered with ice, 30% with rocks, and 10% with vegetation area. This is the only land for some species such as polar bears, Arctic fox, Svalbard Reindeer, Walrus, etc. Climate change has highly affected this area. The average temperature of this region has increased up to 5^{0}C in five decades (Farnsworth et al., 2020). The amount of precipitation in the form of rainfall increases year by year (Vikhamar-Schuler et al., 2016). This research focuses on the North-western part of Svalbard, the glaciers close to Ny-Ålesund. The area of the Ny-Alesund is used as the research base station.

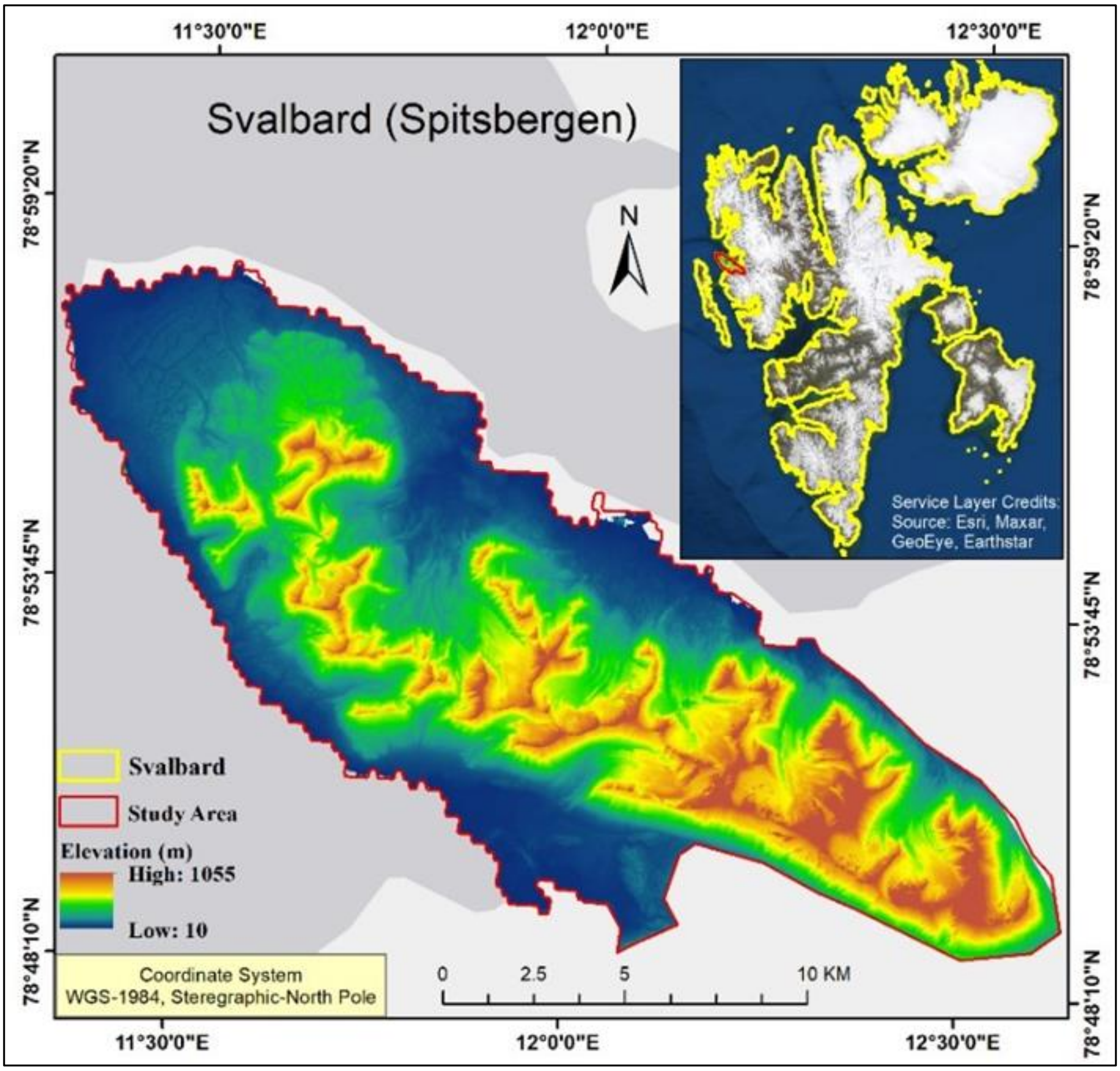

Figure 3.2: Study area site 2, Svalbard

4 DATA AND SOFTWARE

In this study, the data from the European Space Agency (ESA) satellites Sentinel-1 and Sentinel-2 will be exploited to extract information. Both S1 and S2 satellites are ESA initiations under the European Union Copernicus program for earth observation. The data and services are open and freely available to the scientific community. We decided to consider the data from the summer month, as the study area has limited cloud-free optical images. At the same time, the melting seasons can help to identify more glacier surface.

4.1 Sentinel-1

Sentinel-1 is a Synthetic Aperture Radar imaging mission that uses the C-band radar imaging system. The constellation of two satellites, Sentinel-1A, and Sentinel-1B, are placed in the polar orbit with a distance of 180^0. S1 provides the data with the temporal gap of 12-days at the equator, but when we combine both S1a and S1b, it can be achieved up to the interval of six days. Sentinel-1 carries a C-band SAR sensor, which operates in single (HH and VV) and the dull polarization (HH+HV and VV+VH). It acquires data in four different acquisition modes and provides two different products. Single look complex product preserves both phase, and amplitude information, whereas the Ground range detection product only provides amplitude information. This research only explored the VV+VH dual-polarization data, as there was no data in HH+HV polarization mode for the study area. More information about the S1 data is mentioned in Appendix-1 Table1. Data used in this research is mentioned in Table 4.1

Table 4.1: The information of the Sentinel-1 data used in this research

Study Area	Orbit	Acquisition date	Product	Polarization
Svalbard	34001	21-08-2020	SLC-IW	VV VH
Jostedalsbreen	17811	30-08-2019	SLC-IW	VV VH

4.2 Sentinel-2

Sentinel-2 is a multispectral optical imaging mission that provides high-resolution datasets. It is also the constellation of two satellites, S2a, and S2b, like the S1 mission, and placed in a polar orbit with a gap of 1800. The single satellite revisits the same place at the equator while combining products from both sensors, but it is achievable to have the datasets with a gap of five days. Sentinel-2 has twelve spectral bands with 10m, 20m, and 60m of spatial resolution. The optical and infrared bands have 10m spatial resolution (Drusch et al., 2012). This research included all bands of sentinel-2 except the band-10 (Cirrus), as it does not contains surface information. More information about the S2 data is mentioned in appendix-1, table-2. This research used different tiles for the different study areas mentioned in Table 4.2.

Table 4.2: The information of the Sentinel-2 data used in this research

Study Area	Tile number	Acquisition date
Svalbard	T33XVH	25-08-2020
Jostedalsbreen	32VLP, 32VMP	27-08-2019

4.3 GLIMS

Global Land Ice Measurements from Space (GLIMS) is an open database and inventory for glaciers worldwide (National Snow and Ice Data Center, 2005). The GLIMS database stores information such as glacier extent and the movement of the glaciers. The GLIMS database combines satellite products, ancient geographical maps, and ground data from different glaciological organizations worldwide. This project was initiated to provide reliable information to the researchers working on glacier research (Raup et al., 2007). The glacier boundary has been clipped according to the study area.

4.4 Digital Elevation Model

Arctic DEM

Arctic DEM is the output of the United States National geospatial-intelligence Agency (NGA) and National Science Foundation (NSF) collaborative project. This DEM is generated using high-resolution optical stereo images. Although the stereo images for this project are a combination of multiple sensors, the majority of them are from the Worldview series. This product is freely available for the research project, and anyone can download it by visiting this link. ArcticDEM is available from 60^0N and covers the entire arctic region, including Alaska, Greenland, and Svalbard. This research used a 10m product.

TransDEM

TransDEM is available only for Norway, and it is generated using the LIDAR data and is available with 1m of resolution. It is also freely available and can be downloaded using this link. This 1m resolution DEM is further downscaled at 10m to match the sentinel-1 and sentinel-2 pixel size.

4.5 Software and packages

Table 4.3: Software and libraries used to process the data and conduct the research

Software	Function
SNAP	Sentinel-1 data preprocessing Use to resample the sentinel-2 10m, 20m, and 60m at 10m
QGIS	To label and prepare the training dataset
Python	Jupyter notebook is used to implement the FCN
Libraries/Packages	**Function**
TensorFlow	Used to implement and execute FCN
NumPy	For the mathematical function (image to the array)
Matplotlib	Visualization of images and graphs
skimage	For raster image processing
Gdal	To handle and process geospatial data
Focal-loss	Replaces with the TensorFlow loss function

5 METHODOLOGY

5.1 Conceptual framework

As mentioned in section 1.1, glacier mapping and monitoring are essential derivatives for multiple research activities. It is vital to update glacier inventory regularly, but manual and semi-automated methods are time-consuming. Therefore, this study focuses on an FCN method to extract glacier extent. Figure 5-1 shows the conceptual framework for this research. This research implements three approaches to achieve the outputs (Glacier extent).

In Approach-1, the different bands of an optical satellite image (Sentinel-2) work as an input to the fully convolutional neural network architecture. Approach-2, the polarimetric SAR data is considered as an input. The different polarisations of SAR data are used as input layers in fully convolution neural network architecture. In Approach-3, SAR and optical data fusion with the same spatial resolution is used in the input layer of fully convolutional neural network architecture.

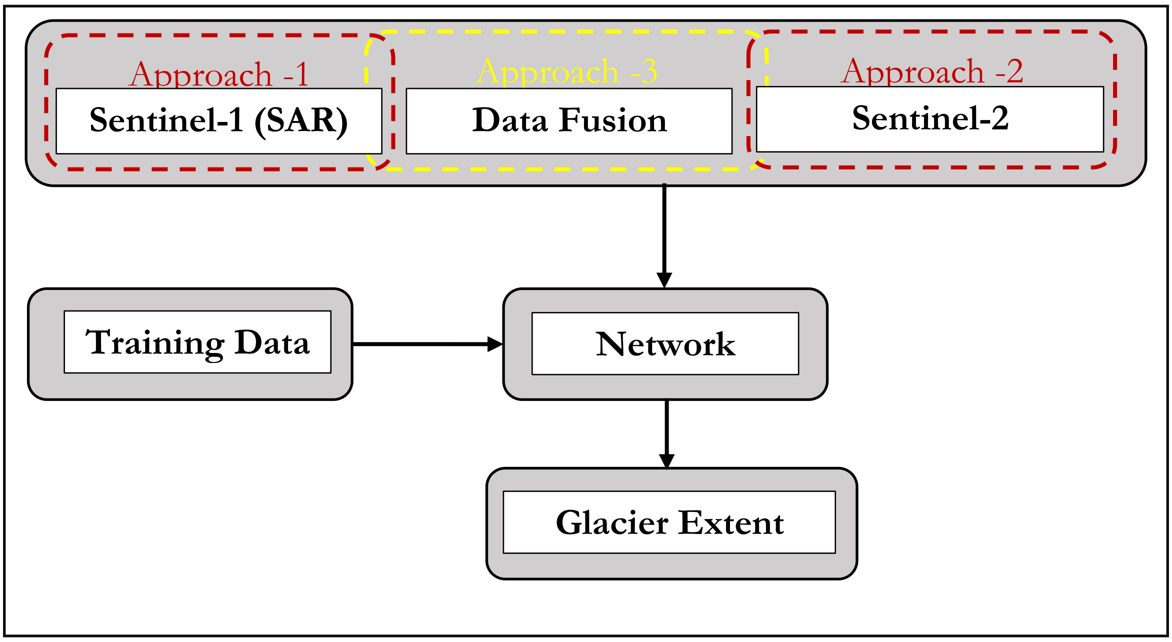

Figure 5.1 : Adopted framework for this research

5.2 Data Pre-processing

5.2.1 Sentinel–1 SAR data

While using the SAR datasets for any application, preprocessing is an important step. In this research, we explore the polarimetric information of the Sentinel-1 data. In most scenarios, polarimetric analysis is done by utilizing its power's backscattered intensities or ratio. Sentinel-1 data has some pre-defined steps while using the data. During this research, we followed these pre-defined steps along with the required steps as per research.

As indicated in the flowchart shown in figure 5-2, We applied TOPSAR co-registration, orbit correction, and radiometric calibration. We used European Space Agency (ESA) SNAP software to process all these steps, including the generation of the covariance matrix and polarimetric decomposition. Each step was followed and mentioned in Figure 5-2. We subdivided these steps into five small steps and processed them using the SNAP graph builder.

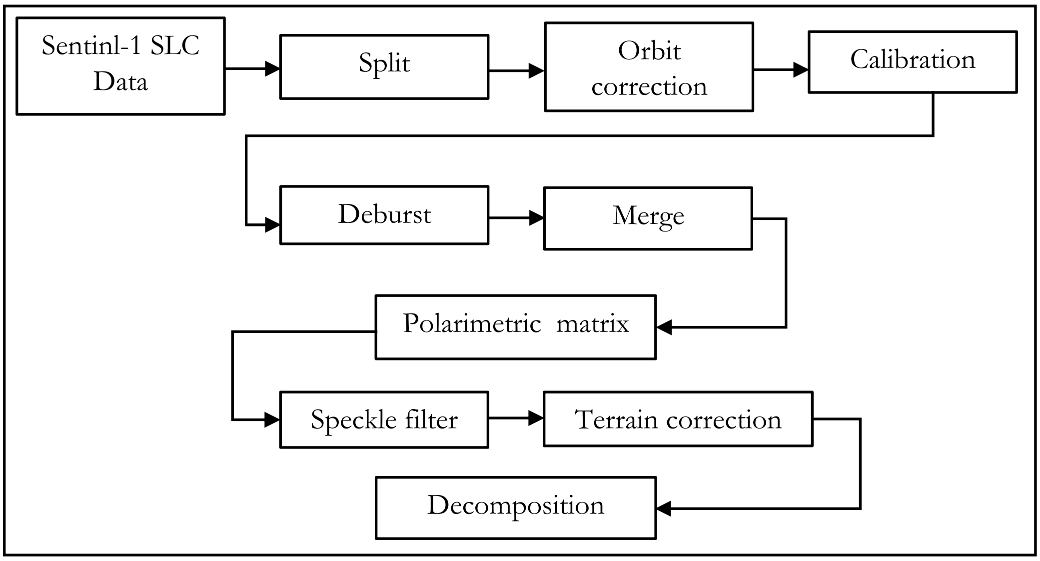

Figure 5.2: Flowchart of the steps followed during the sentinel-1 pre-processing

Sentinel-1 data was captured in three sub-swath, and each sub-swath has nine bursts, so it is recommended to separate each sub-swath using a split tool. After splitting, each sub-swaths orbit file is used to revise the state vector. In our research, we are using both the real and imaginary parts of data, and it is important to save the calibration output as a complex number. In step-2, we combined the multiple sub-swaths and each burst data as per the study area using the Deburst and Merge tool. Later, the covariance matrix for each study area was separately generated using the merged data.

Covariance Matrix

Polarimetric information helps to extract information such as orientation, shape, and dielectric properties using the backscattered from the sentinel-1 data. In sentinel-1, there are dual polarimetric channel, which is VV, and VH. This information about the target is further represented in the 2 x 2 covariance matrix. This study applied a pre-defined C2 method to generate the dual polarimetric covariance matrix.

According to Nielsen et al. (2017), C2 matrix of VV, and VH (dual-pol) Sentinel-1 data, we can generate the diagonal elements with the help of equation-5.1. Here the S_{vv} is a complect backscattering measured by transmitting electromagnetic wave with vertical polarization and receiving the backscattered wave in vertical polarization, S_{vh} is a complect backscattering measured by transmitting electromagnetic wave with vertical polarization and receiving the backscattered wave in horizontal polarization. S_{vv}* is the complex conjugate of S_{vv}, and S_{vh}* is the complex conjugate of S_{vh}.

$$\mathbf{C2} = \begin{bmatrix} S_{vv}\, S_{vv}{}^{*} & S_{vv}\, S_{vh}{}^{*} \\ S_{vh}\, S_{vv}{}^{*} & S_{vh}\, S_{vh}{}^{*} \end{bmatrix} \qquad \textbf{Equation-(5.1)}$$

$$\mathbf{C2} = \begin{bmatrix} |C11| & |C12_{imaginary}| \\ |C12_{real}| & |C22| \end{bmatrix} \qquad \textbf{Equation-(5.2)}$$

From C2 covariance, we get the product of complex and its conjugate of VV as C11, the product of complex and its conjugate of VH as c22, and the product of a complex of VV (VH), and the complex conjugate of VH (VV) as C12imaginery, and C12real, for final output (equation-5.2). Later we used these outputs, C11, C12, and C12real, as three different bands as an input channel of the networks.

Polarimetric Speckle filter

SAR images always need to be cleaned, and it is caused when the backscattered from the target contains the out-of-phase values. Its presence in the images produces noise and degrades the quality of interpreting the images. While preparing the dataset for deep learning, our research observed that the different filtering techniques influence the results. After trial, and error methods, we concluded to apply the Refined Lee filter with the parameters reported in Table 5.1. The after effect of filtering is presented in Figure *5.3.*, the

Table 5.1: Parameter used during the speckle filtering for this research

Name of Speckle Filter	Refined Lee filter
Number of looks	1
Window size	5 x 5

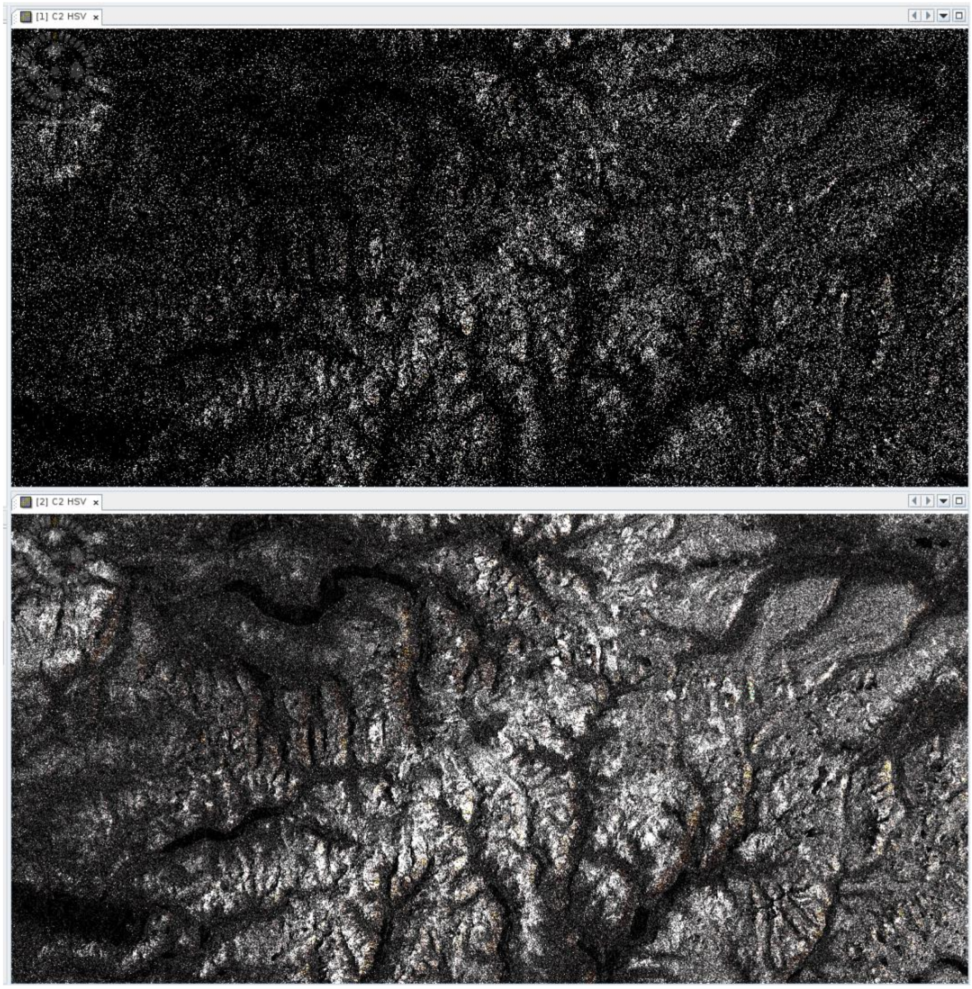

Figure 5.3: The effect of refined lee filter on Jostedalsbreen area. The upper image before filtering and lower images after the filtering.

Terrain correction

The terrain correction converts the radar geometry (which comes in ground range and slant range geometry) into the map coordinates. While implementing the terrain correction, we used an external DEM of 10m (Arctic DEM from Svalbard and Trans DEM for Jostedalsbreen). We also converted ground range pixel geometry into the WGS projection with 10m of pixel spacing. The parameters changed in S1toolbox while terrain correction is mentioned in Table *5.2.*

Table 5.2: Parameters used during the terrain correction

DEM	Arctic DEM from Svalbard, and Trans DEM for Jostedalsbreen
Resampling method	Bilinear interpolation
Pixel spacing (m)	10
Projection	WGS 84

Decomposition
Polarimetric Decomposition permits the distinction of the distinct scattering contributions, and further, it is used to separate information about the scattering process (Cloude and Pottier, 1997). To produce the decomposition, we selected H-A-Alpha dual decomposition from the S1Toolbox, and we again kept the window size 5. Anisotropy, entropy, and Alpha from the decomposition are calculated using the eigenvalues and eigenvectors produced from the polarimetric matrix (Cloude and Pottier, 1997). Alpha gives the angular values and describes the backscattering types, and its value ranges from 0^0 to 90^0. Entropy describes scattering heterogeneity, whereas the Anisotropy complements second- and third-order backscattering mechanisms. These decomposition products, Anisotropy, Entropy, and Alpha, are three other bands (after covariance matrix product |c11|, |c22|, |c12real|) for the input channel of the network.

Exploration of phase information
During this research, we also explored the possibility of Sentinel-1 phase data while considering the relative phase of the VH and VV (arctan2 of $S_{vh} S_{vv}^*$), but later we did not find any relevance considering the deep learning. The image output of this preprocessed was noisy, as shown in figure-5.4. Our first interaction, while considering single SAR image phase information for the study area, was not useful. We decided to stop the further Exploration of considering phase information.

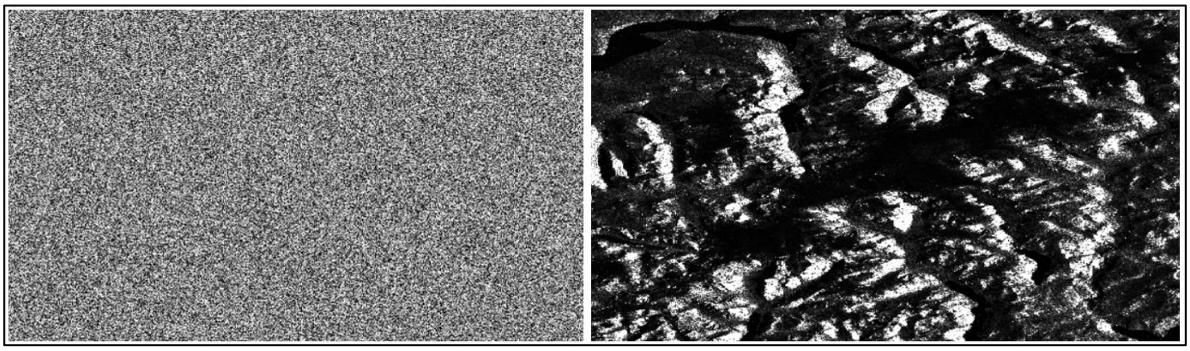

Figure 5.4: a. phase image of the Jostedalsbreen, b. intensity image of the same image-a.

5.2.2 Sentinel-2 Optical data
We downloaded the Sentinel-2 level-2 product via the Copernicus data hub. This level 2 atmospherically corrected product is available at different resolutions, whereas in this research, we are using all spatial resolution data, so we decided to resample all 20m and 60m resolution images to 10m. After resampling all bands on 10m, we merged and clipped the images as the study area. As our study area, Svalbard was covered in one tile of an image, but the Jostedalsbreen was unable to cover in one tile. So we merged two different tiles of the same date and later cropped them as our study area using the QGis software.

5.3 Data preparation for model
We started with the GLIMS(Global Land & Ice Measurement from Space) and NPI (Norwegian Polar Institute) glacier boundary to prepare the dataset. The GLIMS boundary is used for the Jostedalsbreen, whereas the NPI inventory is used for Svalbard. We downloaded these datasets in the form of a vector file as a polygon. This glacier boundary is delineated under expert supervision with the help of field truthiness. The datasets of the GLIMS inventory are available spatially extended throughout the map, so we clipped according to the extent of our region of interest for Jostedalsbreen, and at the same time, we also clipped for Svalbard from the NPI glacier boundary.

Our research conceptualizes the glacier boundary as the outer extent of the glacier area that defines the transition from glacier area to a non-glacier area. We considered all the features which are not fulfilling the definition of the glacier as a non-glacier. In our study region, most non-glacier areas include mountains, vegetation, and water bodies. Our definition of glacier boundary does not include the other side features. It is just a separation between the glacier, and the non-glacier area, which is shown in Figure *5.5*

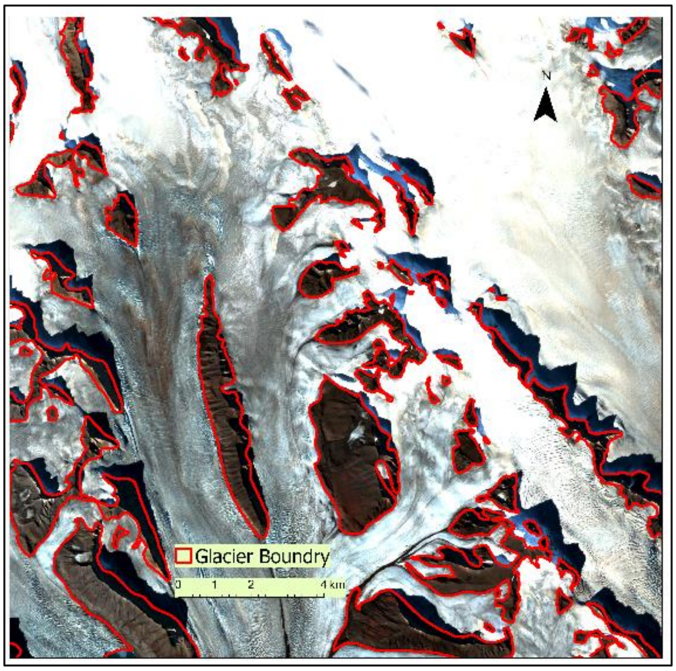

Figure 5.5: Sentinel-2 raw image showing the glacier as a non-glacier area

In the process of data preparation, the first step was the conversion of the reference polygon into a raster form using the "Rasterize" tool of QGIS software. There was consideration for each pixel of the training data representing 10m x 10m of spatial resolution so that it could match the resolution of the Sentinel-2 data. The tool "rasterize" takes the vector file as an input and convert it into raster while assigning all glacier area as value one and non-glacier as zero. After the rasterizing and assigning each pixel as a label, either glacier or the non-glacier, we consider these datasets as labeled data or the labeled image, which is shown in Figure *5.6*.

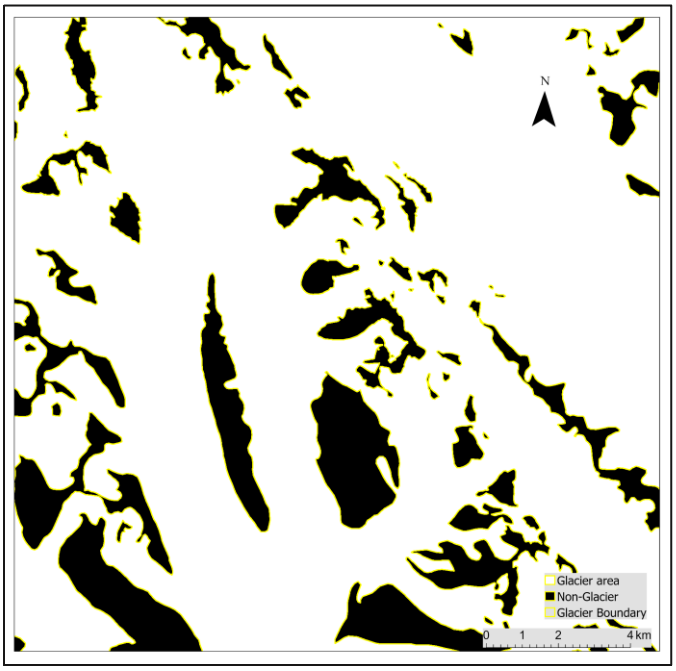

Figure 5.6: Ground truth sample, the assigned label for the glacier is 1, and 0 represents non-glacier

Later in this step, we aligned both the raster images, the labeled as well as sentinel images, with the help of the "align raster" tool of QGis. This tool can bring multiple raster files together and perfectly align them, which means both the raster assigned the same projection, resampled with the same pixel size, and overlaid to the same extent. While defining the resampling parameter, we used the bilinear resampling method of *2* *x 2* kernel size. Our study area is individual of *8595 x 8595* pixels, where each pixel represents *10m x 10m* of spatial resolution.

Later in the next step, we used this referenced data and raw images and divided them into the network's training, validating, and testing. The image of Svalbard and Jostedalsbreen has 8595 x 8595 pixels, so we divided it equally into 25 tiles, where each tile has subsequent ground truth and raw images of sentinel with the same area coverage. Sentinel-1, sentinel-2, and fusion data covered the same spatial coverage. After the division of images into 25 tiles, we ended each tile with *1719 x 1719* pixels. The tiles indication for each study area is shown in Figure *5.7*, Figure *5.8*, Figure *5.9*, and Figure *5.10*.

Later we combined train tiles, validate tiles, and test tiles from both study areas to train, validate, and test the model. The combination of train, validate, and the test is the same throughout the research.

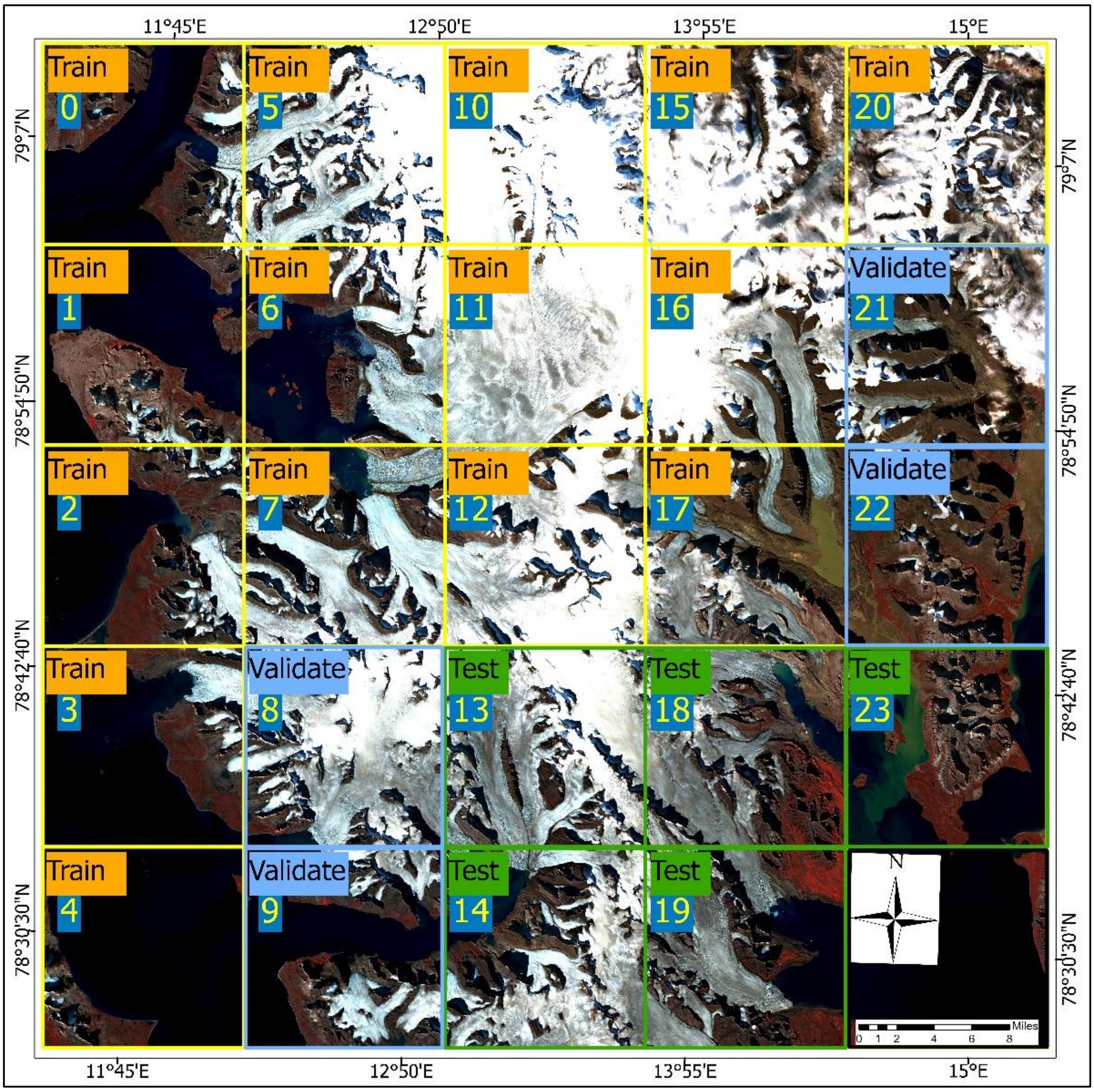

Figure 5.7 : Tiles for training, validation, and testing for Svalbard; this tile number is applicable for Sentinel-1, Sentinel-2, and fusion datasets.

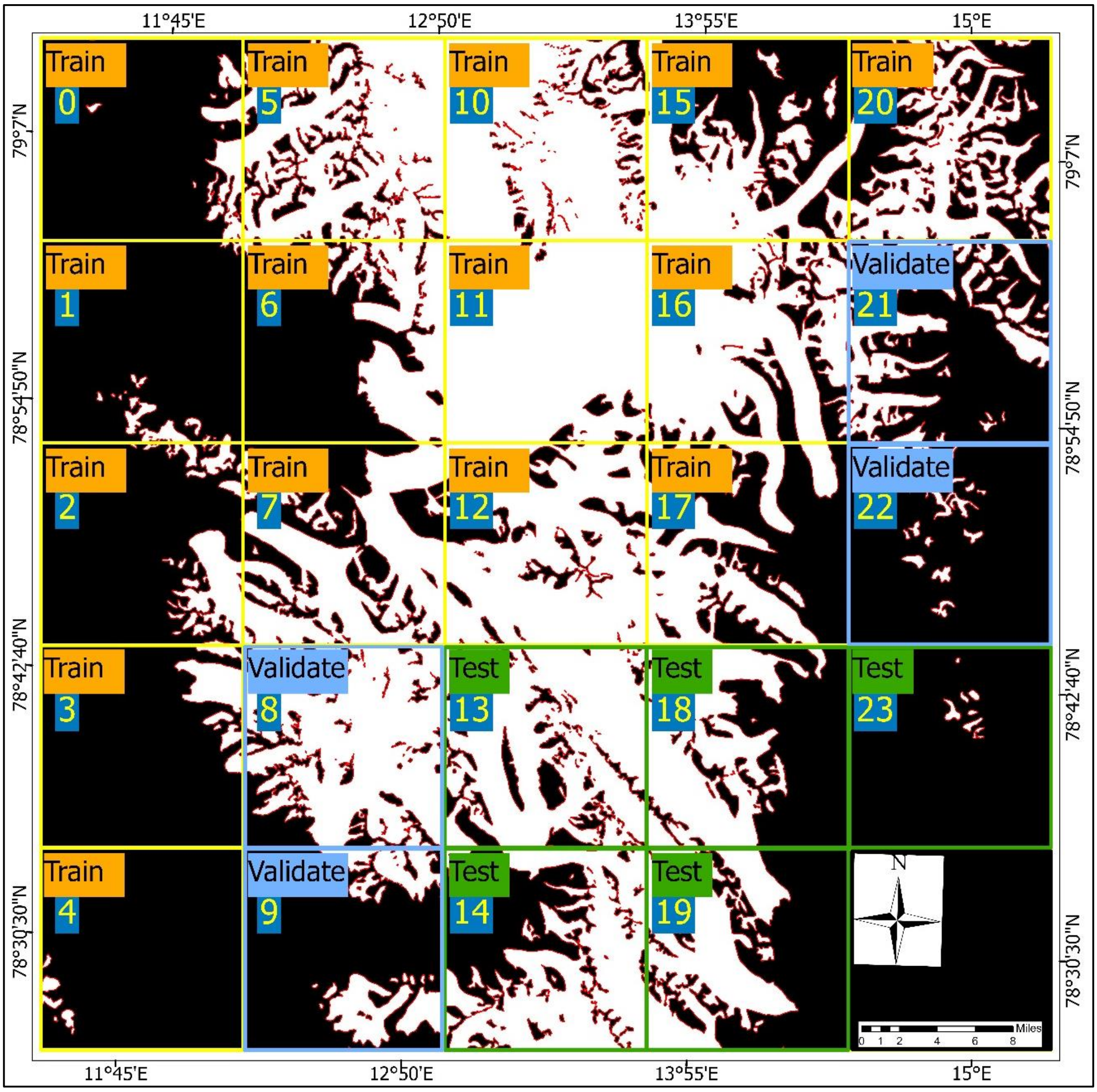

Figure 5.8: Ground truth tiles for Svalbard. This is 'train' and 'validate' for training, and validation of network, and 'test' for testing

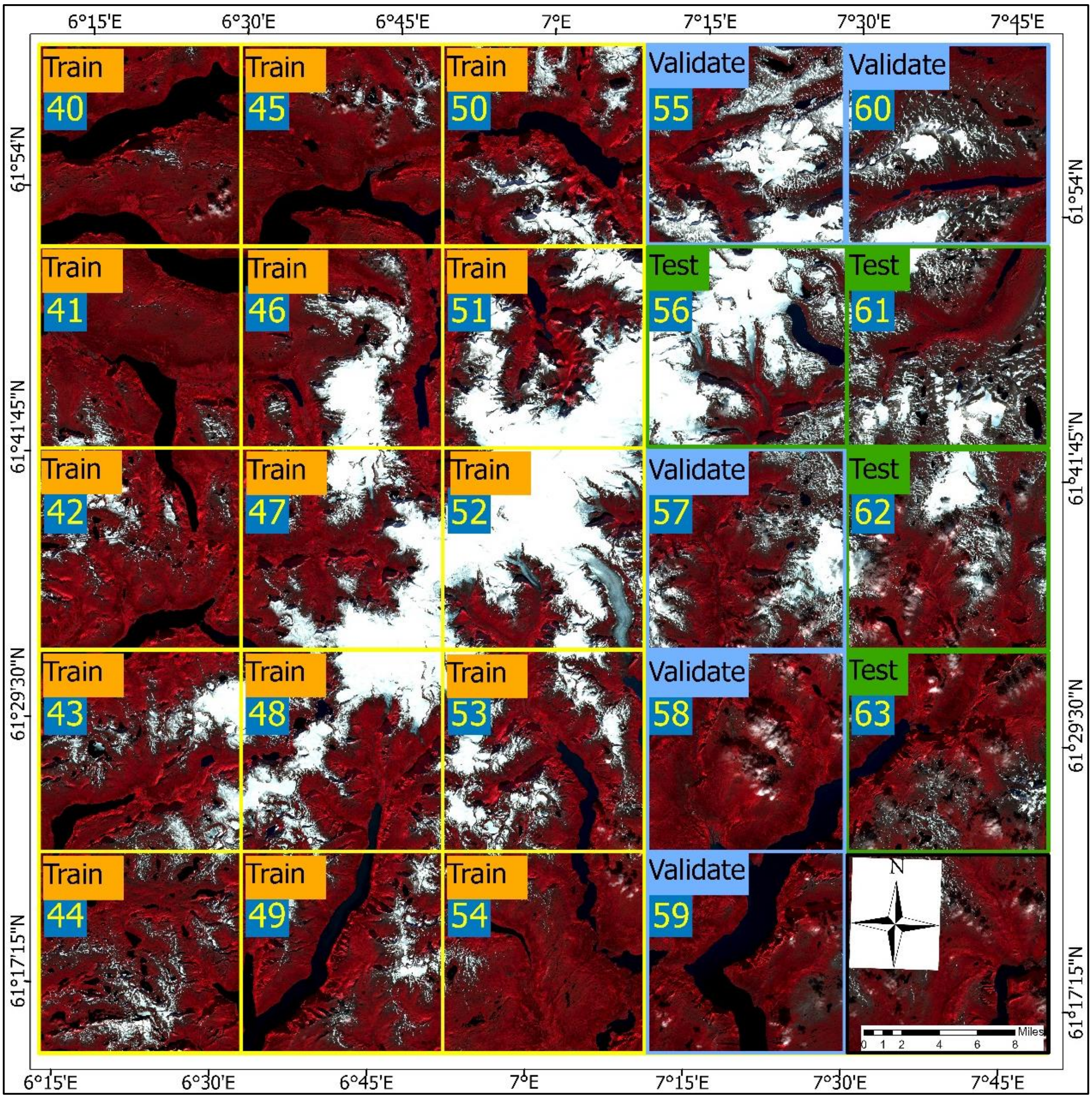

Figure 5.9: Tiles for training, validating, and testing for Jostedalsbreen. This tile number is applicable for Sentinel-1, Sentinel-2, and fusion data.

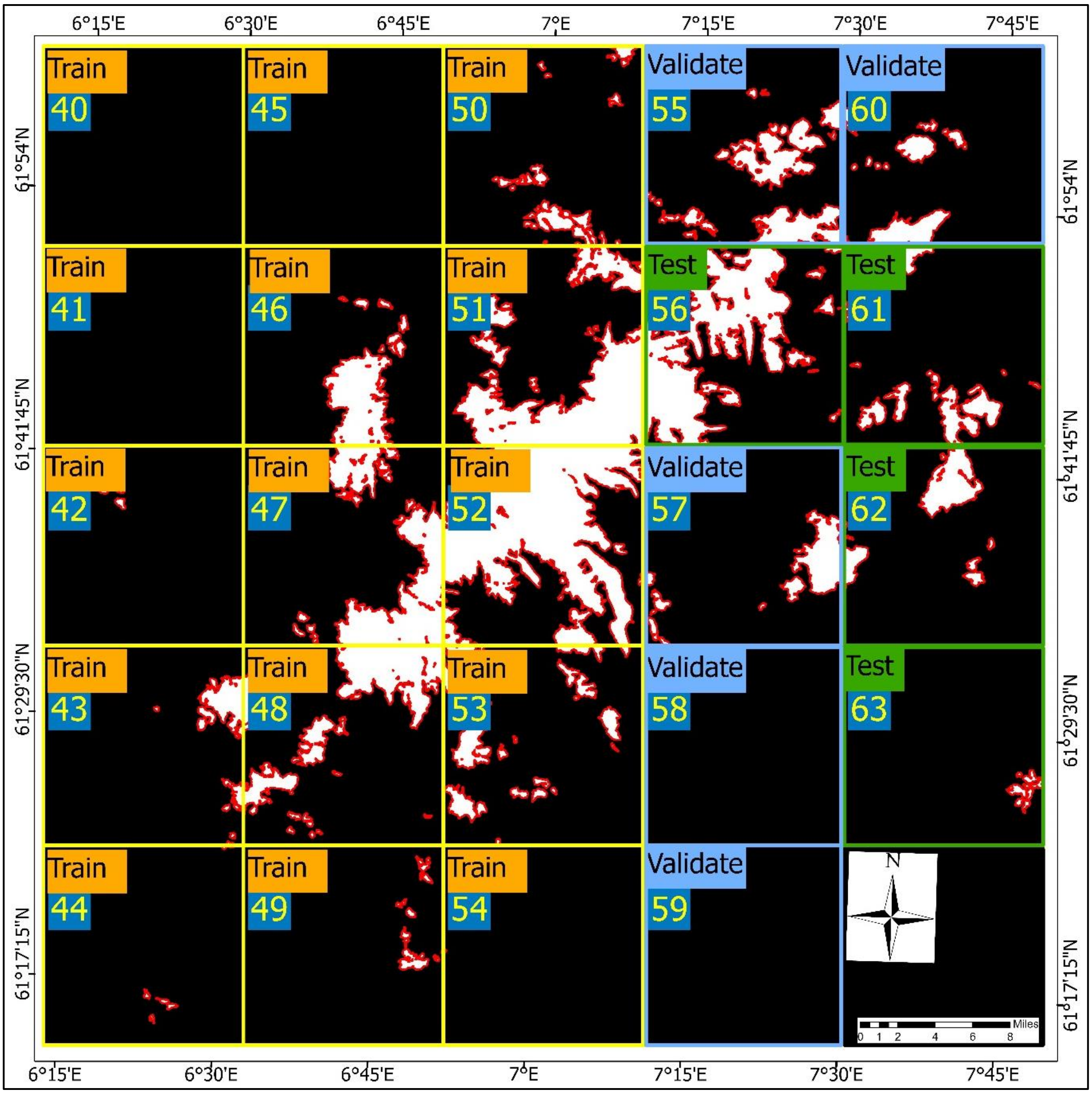

Figure 5.10: Ground truth tiles for the Jostedalsbreen. This is to train and validate if for training, and validation of network and 'test' is for testing

5.4 Deep Learning Networks

5.4.1 FCNDK

The fully convolution neural network is a pixel-based classification method and is also known as semantic segmentation. This semantic segmentation approach FCN-DK was first proposed by (Persello and Stein, 2017). This network was used to detect informal settlements using very high resolution (VHR) satellite images with high accuracy. This (Persello and Stein, 2017) proposed this novel architecture, convolution layer as a main block of the network, to reduce the large spatial parameter dependency while adopting the convolution with diluted kernels. In this architecture, there are six convolution layers with dilated kernel, leaky ReLu, and max-pooling. The final layer for classification consists of convolution layer and softmax loss function, the full architecture of this network is shown in Table *5.3*.

Table 5.3: Architecture of FCN DK-6

Layer	Module type	Dimension	Dilation	Stride	Pad
DK 1	Convolution	5 x 5 x 4 x 16	1	1	2
	1ReLU				
	Max-pool	5 x 5		1	2
DK 2	Convolution	5 x 5 x 4 x 16	2	1	4
	1ReLU				
	Max-pool	5 x 5		1	4
DK 3	Convolution	5 x 5 x 4 x 16	3	1	6
	1ReLU				
	Max-pool	5 x 5		1	6
DK 4	Convolution	5 x 5 x 4 x 16	4	1	8
	1ReLU				
	Max-pool	5 x 5		1	8
DK 5	Convolution	5 x 5 x 4 x 16	5	1	10
	1ReLU				
	Max-pool	21 x 21		1	10
DK 6	Convolution	5 x 5 x 4 x 16	6	1	12
	1ReLU				
	Max-pool	25 x 25		1	12
Classification	Convolution	1 x 1 32 x 2	1	1	0
	SoftMax				

5.4.2 SegNet

Another example of the semantic segmentation architecture is SegNet (Figure *5.11*), which is designed to work efficiently for "pixel-wise semantic segmentation" (Badrinarayanan et al., 2017). This architecture works with the concept of an encoder-decoder-based network, where each encoder is hierarchically connected with its corresponding decoder. The encoder pat of this network is identically based on VGG16 (Simonyan & Zisserman, 2018) network. The encoder network consists of layers of the convolution along with batch normalization and ReLu, to extract the features, whereas the decoder helps to improve the low-resolution feature by upsampling, pooled from the encoder. The final layer of the decoder consists of a softmax classifier.

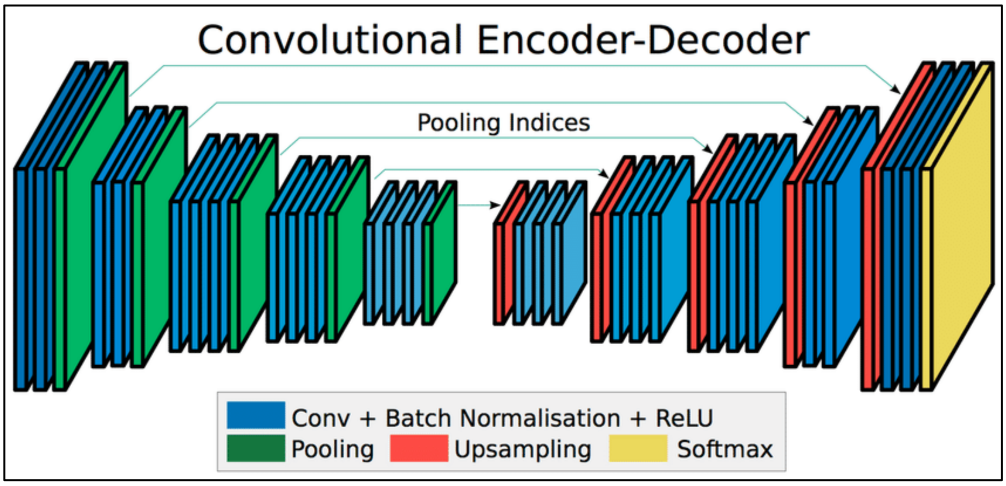

Figure 5.11: The architecture of original SegNet, source: (Badrinarayanan et al., 2017)

5.4.3 UNet

U-Net is a deep learning network for image segmentation, originally developed to study the biomedical-images. It is divided into two sides contracting and expansive. Originally, the contracting part consisted of 3 x 3 unpadded convolutions followed by ReLu, and 2 x 2 max-pooling, whereas the expansive part also includes the 3 x 3 convolution layer along with the upsampling layer of 2 x 2 up-convolution. The last layer of the network has a 1 x 1 convolution layer (Ronneberger et al., 2015), as shown in Figure 5.12.

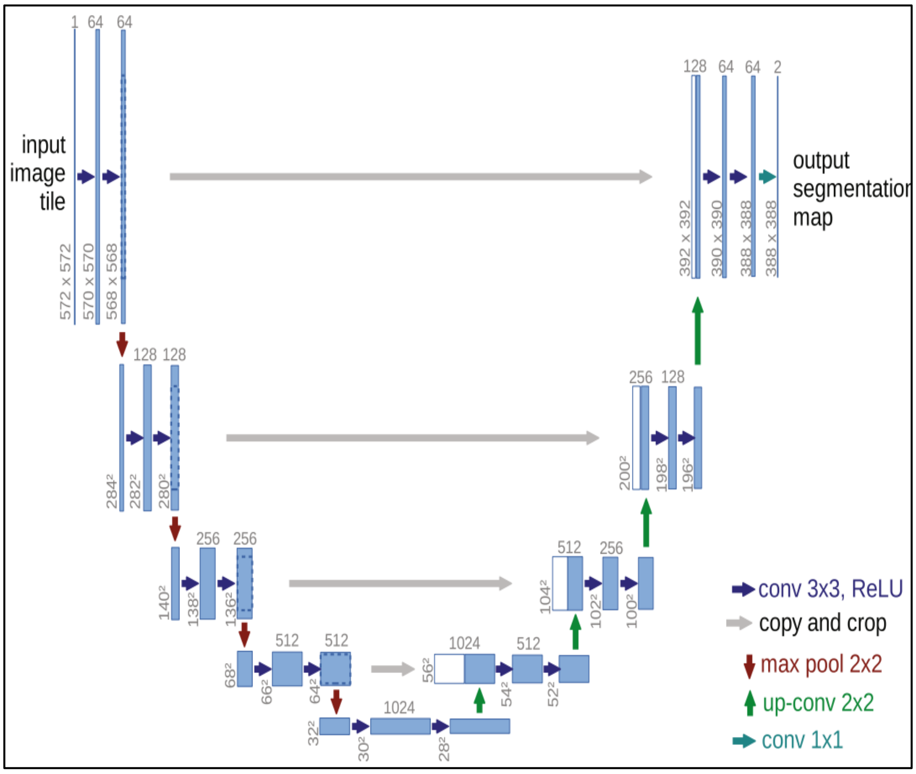

Figure 5.12: Architecture of the U-Net developed by (Ronneberger et al., 2015)

5.4.4 ResUnet

ResU-Net architecturally combination of residual network and UNet. This network used the twofold concept. First, it replaces the plain neural unit with the residual unit, and second, removal of cropping operation, which helps the network with improved performance and refined architecture. This network also works with the encoder-decoder principle; it has three parts a) encode, b) bridge, and c) decoder. Every part of the network has its residual unit with a convolution block of 3 x 3 units, where each block of convolution includes a layer of batch normalization, an activation function ReLu, and convolution. The schematic diagram of the network is shown in Figure *5.13*. In our encoder block of all three residuals, we used strides of 2 instead of max-pooling to reduce the feature dimensionality. On the decoder side, we concatenated the feature maps from upsampling and corresponding encoder and added them to the corresponding residual unit. At the end of the network, we added a 1x1 convolution layer followed by an activation layer to have the final output.

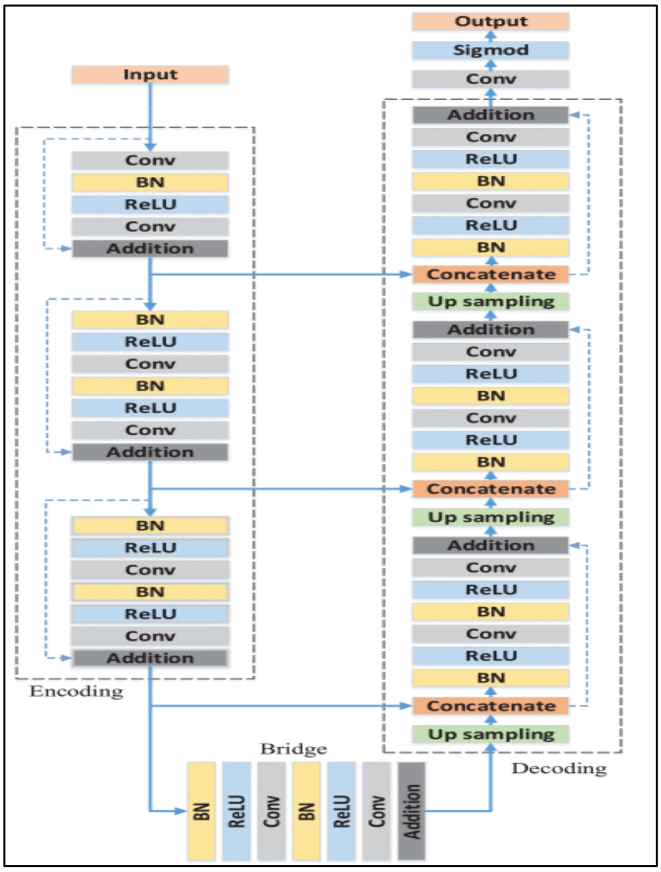

Figure 5.13: Architecture of ResUnet (Zhang et al., 2018)

5.5 Fusion Network

We adopted the traditional fusion technique called early fusion in our fusion network. At the beginning of the data preprocessing, we applied some correction methods separately on Sentinel-1 SAR and Sentinel-2 optical data. Later in the final steps of data post preprocessing, we combined the Sentinel-1 and Sentinel-2 data and generated stacked bands of images out of the networks. These all bands are of the same spatial resolution and are used to extract spatial features and classify inside the different FCNs. Figure *5.14* is the proposed architecture of the network used in this study.

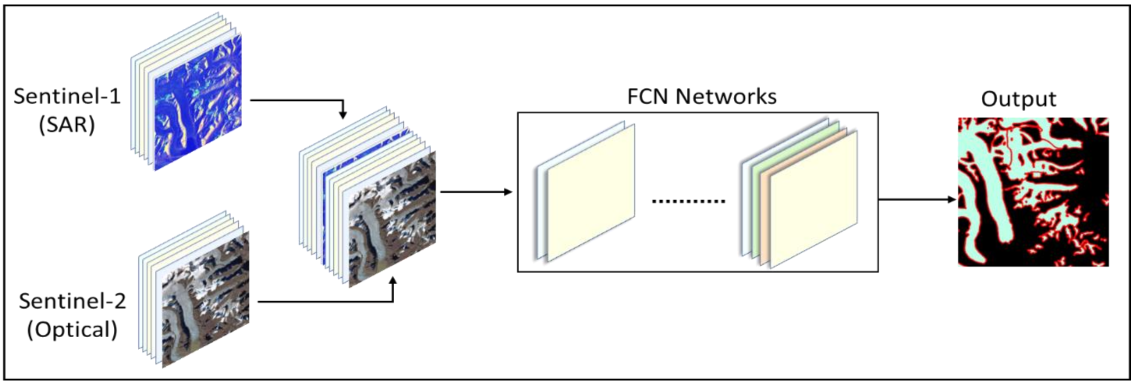

Figure 5.14: Architecture of Fusion network

5.6 Methods for Accuracy Assessment

In general, the base evaluation matrix to evaluate the performance of the Model is Accuracy (A) (equation 5.3). Accuracy describes the ratio of correct prediction and all predictions. But In this research, the F1 score is considered the evaluation standard to measure the performance of all networks. F1 (equation 5.6) describes the harmonic mean of the precision (p) and recall (r) (Chicco and Jurman, 2020). It describes additional appropriateness to the ratios than the conventional mean. F1 varies between 0-1, where 0 signifies the bad performance, and 1 depicts the best performance. We also considered precision, and recall, as precision (equation 5.5) shows the truthiness and the quality of the result. Recall (equation 5.4) analyzes the sensitivity and quantifies the qualitative aspect of the correctly predicted pixel. The base of this evaluation depends on the four components false negative, false positive, true negative, and true positive. These components are described in Table *5.4*.

Table 5.4: F-score components for accuracy assessment

Accuracy terms	Specification with glacier boundary
True Positive (Tp)	The pixel of the glacier area was correctly predicted.
True Negative (Tn)	The pixel of the glacier area was correctly rejected.
False-positive (Fp)	The pixel of the non-glacier area is predicted as a glacier area.
False-negative (Fn)	The pixel of the glacier area is predicted as a non-glacier area.

Accuracy signifies the all correctly predicted glacier, and non-glacier pixel over the total pixel

$$A = \frac{Tp+Tn}{Tp+Tn+Fp+Fn} \qquad \text{Equation 5.3}$$

$$\text{Recall (r)} = \frac{Tp}{Tp+Fn} \qquad \text{Equation 5.4}$$

$$\text{Precision (p)} = \frac{Tp}{Tp+Fp} \qquad \text{Equation 5.5}$$

$$F1 = 2 * \frac{p*r}{p+r} \qquad \text{Equation 5.6}$$

6 EXPERIMENT AND RESULT

In this chapter, we are describing the experimental setups and their results with analysis. We designed this research in a way so that we can explore Sentinel-1 and Sentinel-2 datasets separately before fusing them. We started our experiment with Sentinel-1 SAR data, followed by Sentinel-2 optical data, and at last, we applied the fusion of both datasets. These three datasets are further trailed with four different generic deep learning networks. This chapter explains all these experimental setups, including their outputs. This chapter is divided into four different sections. First explains the use of FCNDK, SegNet, UNet, and ResUnet with the sentinel-1 data. The second describes the experiment setup with Sentinel-2 data. In the third section, we covered the results and performance of the fusion method. At last, in the fourth section, we explained and compared all results.

Tuning with the learning rate

Before digging into the main experiment, we decided to have a preliminary analysis to set a proper base for all networks. We first executed the FCN network with a single study area FCNDK-6 with different hyperparameter combinations. At a very early step, the network was trailed with a different learning rate (lr), as it is an important hyperparameter that helps to tune the model with respect to the error while updating the model weight. We started to train our network with a learning rate of 10^{-2} and checked till 10^{-6}. Lowering the learning rate was time-consuming, and we did not see any improvement in the F1 score. The result with different learning rates is mentioned in Table *6.1*. We decided to continue our experiment with learning rates of 10^{-4} for optical data and 10^{-5} with SAR data, respectively.

Table 6.1: Results of network with different learning rates (lr)

		lr = 0.01	lr = 0.001	lr = 0.0001	lr = 0.00001	lr = 0.000001
Optical	Accuracy	0,9796	0,9136	0,9894	0,9879	0,9710
	Recall	0,8543	0,7879	0,8793	0,8850	0,8750
	Precision	0,9644	0,9609	0,9780	0,9509	0,9640
	F1	0,8861	0,8580	**0,9260**	0,9168	0,9010
SAR	Accuracy	0,8924	0,9023	0,9488	0,9554	0,9374
	Recall	0,6422	0,7106	0,7229	0,7581	0,6974
	Precision	0,7263	0,7474	0,7692	0,8009	0,8951
	F1	0,6761	0,7134	0,7453	**0,7789**	0,7454

Comparison between different loss function

For the glacier boundary, we also decided to check another factor, which is a different loss function, as it contributes to updating the weights for the network. We decided to check with cross-entropy loss and its improved version, i.e., focal loss (here, we used Binary focal loss (BFL)). But we found the SAR has higher accuracy with cross-entropy loss, whereas optical was better performing with cross-entropy. We decided to run all the networks with both loss functions at least once. The comparative result of both the loss function is mentioned in Table *6.2*.

Table 6.2: Results of network with cross-entropy loss and binary loss function(BFL)

	Optical		SAR	
	Cross-entropy	Binary Focal loss (BFL)	Cross-entropy	Binary Focal loss (BFL)
Accuracy	0,9744	0,9718	0,9327	0,9231
Recall	0,8394	0,8041	0,7486	0,7887
Precision	0,8805	0,9628	0,7387	0,7181
F1	0,8306	**0,8529**	**0,7376**	0,7301

Considering different band combinations

The sentinel-1 and sentinel-2 come with different products, and considering this factor, we decided to make different combinations of bands and check with all networks to have higher accuracies. The visual of the glacier boundary with all three data combinations is shown in Figure *6.1*, and a small analysis is explained.

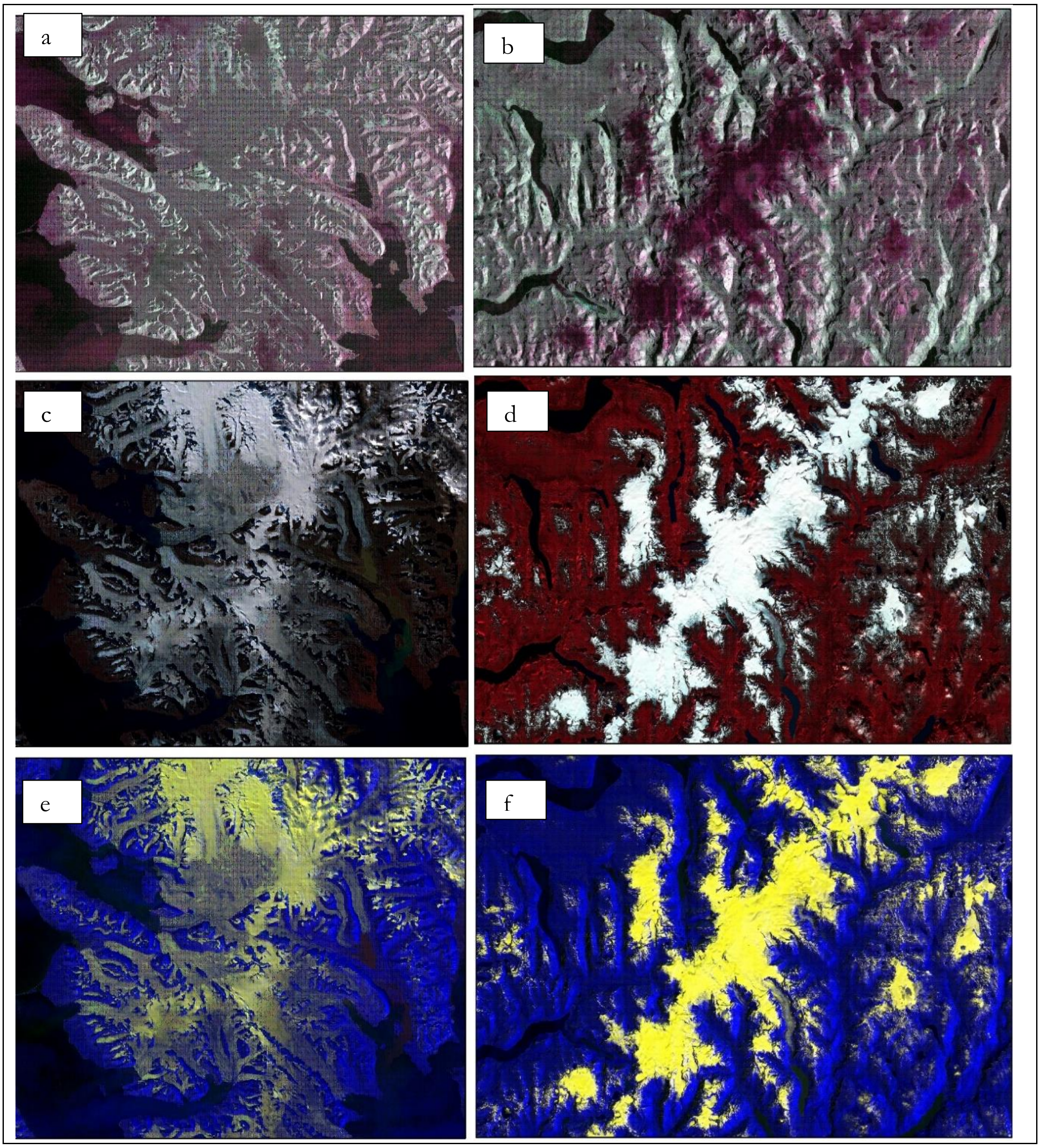

Figure 6.1: The visual of glacier area, 1a) shows Svalbard with Sentinel-1 bands (VV, VH, VV+VH), b) shows Jostedalsbreen with Sentinel-1 bands (VV, VH, VV+VH), c) shows Svalbard with Sentinel-2 (NIR-R-G) bands, d) shows Jostedalsbreen with Sentinel-2 (NIR- R-G) bands, e) shows Svalbard with Sentinel-1, and sentinel-2 (VV-NIR-G) bands, f). shows Jostedalsbreen with Sentinel-1, and sentinel-2 (VV-NIR-G)

This image is a visualization of the glacier area of both research sites, image-a is of Svalbard, and image-b is of Jostedalsbreen. Image-1 is of Sentinel-1 with a band combination of VV, VH, and VV+VH. Image-2 is a combination of NIR, Red, and Green bands of Sentinel-2. Image-3 is a fusion product of S-1 and S-2, and it is a combination of red, green, and VH. Here can be observed the complexity and simplicity of the glacier area view. Hence, we explored the different band combinations in the FCN network.

6.1 Sentinel-1 experiment

An experiment with sentinel-1 was conducted with the two different setups; first, we executed with a three-band combination, and secondly, with six band combination. Both setups were further performed with four different deep learning networks, which are FCN-DK6, SegNet, UNet, and ResUnet. We used the hyperparameter where the learning rate is 10^{-5}, the patch size is 128, the batch size is 32, and epochs were set for early stopping with validation loss monitoring, with thirty patience, and considered the best one.

6.1.1 Experiment with 3-band

In our experiment with the sentinel-1 data, we started to explore different band combinations, and these bands are generated using the VV, and VH, dual-polarization. First, we generated three bands using the covariance matrix explained in section - 5.2.1. This matrix is generated in equation 5.2 as an output in a 2x2 matrix, three with real values (|C11|, |C12|, and |C12|) and one with complex values (C12). Here we only considered the three intensity channels |C11|, |C12|, and |C12| for our network, whereas C11 as band -1, C22 as band-2, and C12 as band-3. We implemented these bands as an input channel in all four networks, FCN-DK6, SegNet, UNet, and ResUnet. We run all four networks five times to investigate the output uncertainty and included the best results. While comparing all four networks, we found that UNet with the cross-entropy loss function gives the highest F-Score accuracy. The performance of the SegNet was not consistent and ended with the lowest F-Score among all four networks. The best result of each network is mentioned in Table *6.3*. This result comprises the cumulative of all tiles, where each accuracy component is the mean of that component of all tiles.

Table 6.3: Accuracy results of different networks from Sentinel-1 3band input

	FCN DK6		SegNet		UNet		ResUnet	
	Cross Entropy	BFL	Cross Entropy	BFL	Cross Entropy	BFL	Cross Entropy	BFL
Accuracy	0,9327	0,9231	0,6569	0,7047	0,9365	0,9301	0,9023	0,8924
Recall	0,7486	0,7887	0,8072	0,8136	0,7631	0,7526	0,7106	0,6422
Precision	0,7387	0,7181	0,4412	0,4653	0,7515	0,7465	0,7474	0,7263
F1	0,7376	0,7301	0,4916	0,5070	**0,7507**	0,7366	0,7134	0,6761

6.1.1.1 Result analysis of 3-band experiment

The qualitative analysis of the 3-band experiment was done on the basis of visual interpretation. Figure 6-3(results with cross-entropy loss function) shows the output from all networks of tile-14 (RGB combination shown in Figure *6.2*).

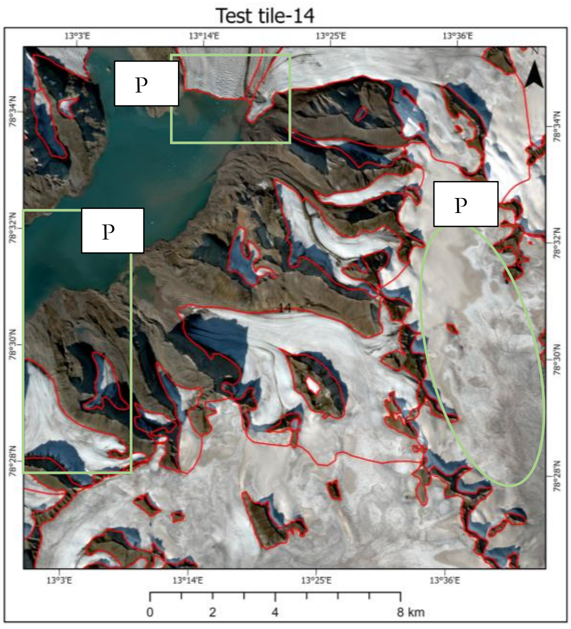

Figure 6.2: Test til-14 (Sentinel-2 4-3-2 band combination)

In this figure, we highlighted three different points, p1, p2, and p3, to show the extreme variance in the output from a different model. The green rectangle of Point' p1' connects to the fjord, and the area has mostly broken ice structure, as shown in Figure *6.3*. This point (p1) is underperformed in results in all networks and is unable to map the boundary accurately. Some area of the fjord, shown at point p2, which is flowing water, is partially segmented as a glacier area by all networks. Point' p3' highlighted in oval structure, which is mostly glacier area, is segmented as a non-glacier area by all networks except UNet. Even with the single test tile (tile-14), it can be clearly seen that the variation in the segmentation result from the SegNet(which has the lowest f1 score) and UNet(highest f1 score). Here, SegNet has overestimated the glacier area and included the non-glacier region in the glacier. Although the UNet has better accuracy, the water pixel inside the glacier boundary is segmented.

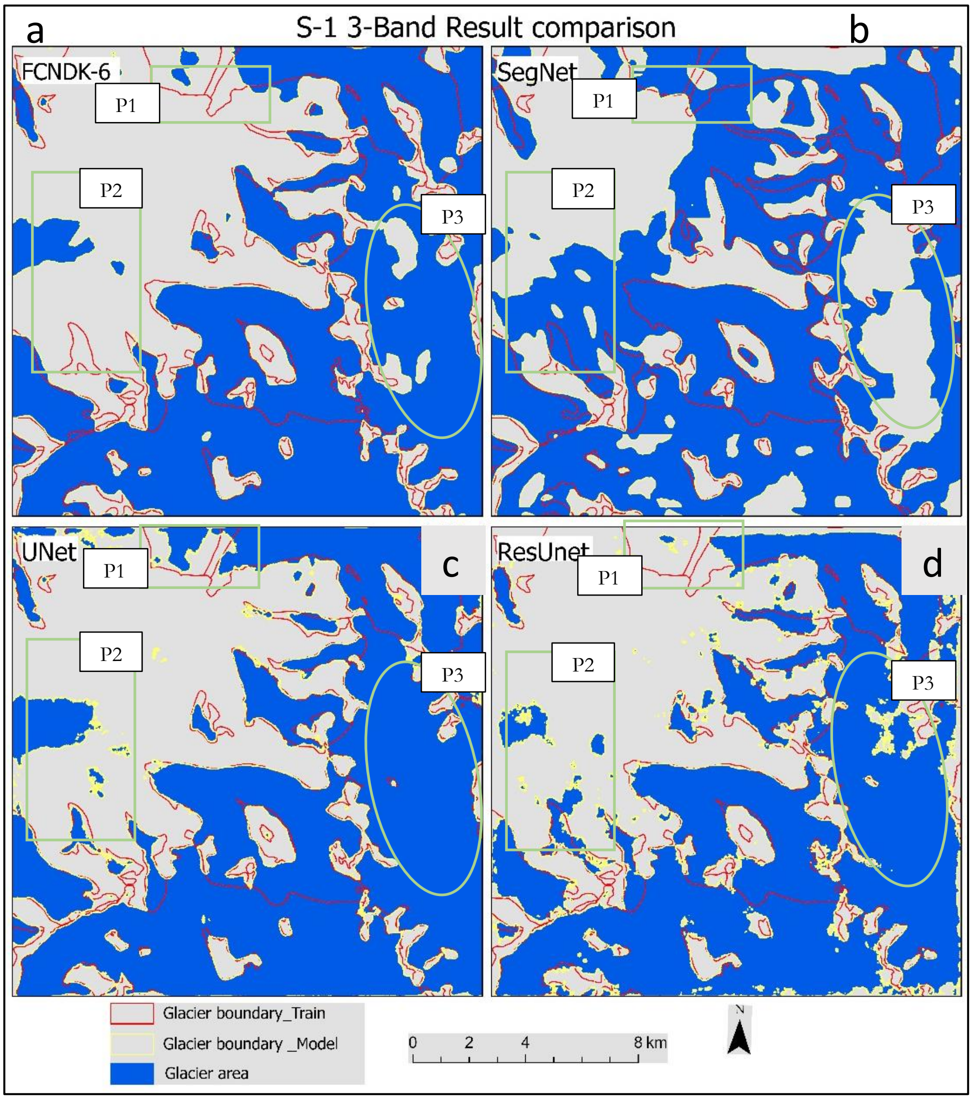

Figure 6.3: Sentinel-1 three-band results from all models. The visuals are the out-of-cross-entropy loss function. a. is the result of FCNDK-6, b. shows the output of SegNet, c. is the output of UNet and d. is ResUnet output

6.1.2 Experiment with 6-band

During the experiment with the six-band combination, we included all three bands used in the 3-band experiment. We added three more bands generated with the polarimetric decomposition method mentioned in section 5.2.1. These bands are capable of differentiating the features on the basis of the scattering mechanism. Three bands, Entropy, Anisotropy, and Alpha, were later combined with C11, C22, and C12real. We considered these six bands as an input in each network where C11 is band-1, C22 is band-2, C12 real is band-3, entropy is band-4, Anisotropy is band-5, and Alpha is band-6. Our evaluation of the experiment with the 6-band of all networks is mentioned in Table *6.4*. UNet with 0.7442 shows the highest F-score among all networks after the five consecutive runs of the experiment.

Table 6.4: Accuracy results of different networks from Sentinel-1 6-band input

	FCN DK6		SegNet		UNet		ResUnet	
	Cross Entropy	BFL	Cross Entropy	BFL	Cross Entropy	BFL	Cross Entropy	BFL
Accuracy	0,9307	0,9374	0,7321	0,6904	0,9317	0,8897	0,8866	0,9020
Recall	0,7267	0,6974	0,3383	0,3995	0,7354	0,7265	0,6915	0,6802
Precision	0,7850	0,8551	0,6674	0,5044	0,7666	0,6766	0,6875	0,7347
F1	0,7328	0,7354	0,3996	0,3300	**0,7442**	0,6826	0,6687	0,6991

6.1.2.1 Result analysis of 6-band experiment

Figure 6-4 shows the qualitative performance of all networks with the cross-entropy loss function of the 6-band experiment. The output from the SegNet shows the underperformance while segmenting the glacier area; the majority of the region, that is glacier area, has been misclassified as non-glacier. Comparatively, UNet performed with better segmentation but was still unable to properly differentiate water area from glacier region, as highlighted in point 'p1' of Figure *6.4*. Some regions, such as point 'p2' of figure 6-4, are glacier areas, resulting in a non-glacier area.

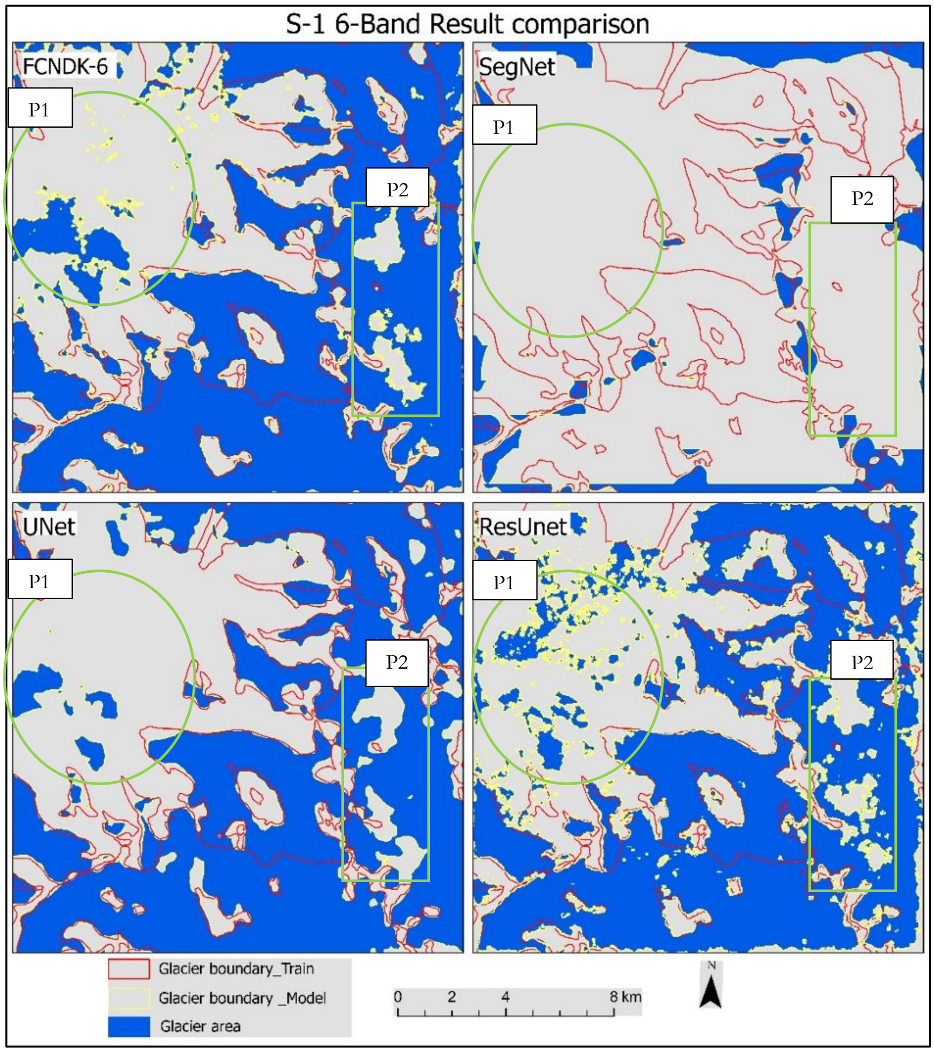

Figure 6.4: Sentinel-1 six band results from all models, the visuals are the out from cross-entropy loss function. a. is the result of FCNDK-6, b. shows the output of SegNet, c. is an output of UNet and d. is ResUnet output

6.2 Sentinel-2 experiment

The experiment setup of sentinel-2 was organized with two different network inputs. First, we used all four bands of sentinel-2 with 10m of spatial resolution and called the 4-band experiment. Second, we introduced all bands of sentinel-2 collectively and named the 12-band experiment. In a 12-band experiment, we resampled bands with 20m and 60m of spatial resolution with 10m. Although the sentinel-2 has 13 bands, we excluded the cirrus band as it does not has surface information. In both experimental setups, we runed with FCN-DK6, SegNet, UNet, and ResUnet. We tuned all DL networks with some common hypermeter, such as learning rate- 10^{-4}, patch size – 128, epochs were set to early stopping while monitoring validation loss with thirty patience.

6.2.1 Experiment with 4-band

First, we investigated the combination of four optical bands, blue, green, red, and near-infrared (NIR) of sentinel-2. These four bands are captured with 10m of spatial resolution and are comparatively considered high-resolution images. The combination of red, green, and blue (RGB) channels makes human eyes capable of easily differentiating the features, but some features only get highlighted if we combine with NIR and make the channel false-color composite (FCC). In this scenario of an experiment, we provided all four bands to the network as an input. As we used a stochastic gradient optimizer, it is important to run the network multiple times to check the network stability. In this experiment, we used an improved version of the stochastic gradient optimizer called "Adam," so we run all our networks five times, and the best result is mentioned in Table *6.5*. We found all network has significant result and are able to segment glacier area with good accuracy, but ResUnet with cross-entropy loss performed best, although the stability among the different was better performed with UNet.

Table 6.5: Result of experiments with 4-bands of Sentinel-2

	FCN DK6		SegNet		UNet		ResUnet	
	Cross Entropy	BFL	Cross Entropy	BFL	Cross Entropy	BFL	Cross Entropy	BFL
Accuracy	0,9744	0,9718	0,9136	0,9772	0,9759	0,9744	0,9796	0,9774
Recall	0,8394	0,8041	0,7879	0,7773	0,8369	0,7815	0,8543	0,8033
Precision	0,8805	0,9628	0,9609	0,8992	0,9645	0,9802	0,9644	0,9754
F1	0,8306	0,8529	0,8580	0,8129	0,8809	0,8310	**0,8861**	0,8514

6.2.1.1 Result analysis of 4-band experiment

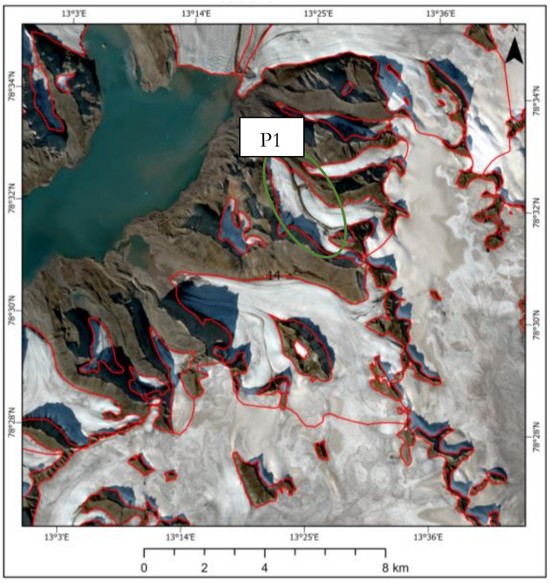

Figure 6.5: Sentinel-2 R-G-B band combination, the glacier boundary of the red outline is overlapped with the glacier area

Figure 6-6 shows the result of all networks from the 4-band experiment. Most of the bigger areas of glacier and non-glacier regions are accurately segmented. But, we observed that there are some small regions that are misclassified. As we highlighted the one region from the test tile-13(shown in Figure *6.5*), point p1 of Figure *6.6*, a tiny portion of the glacier area is separately demarcated as a glacier boundary.

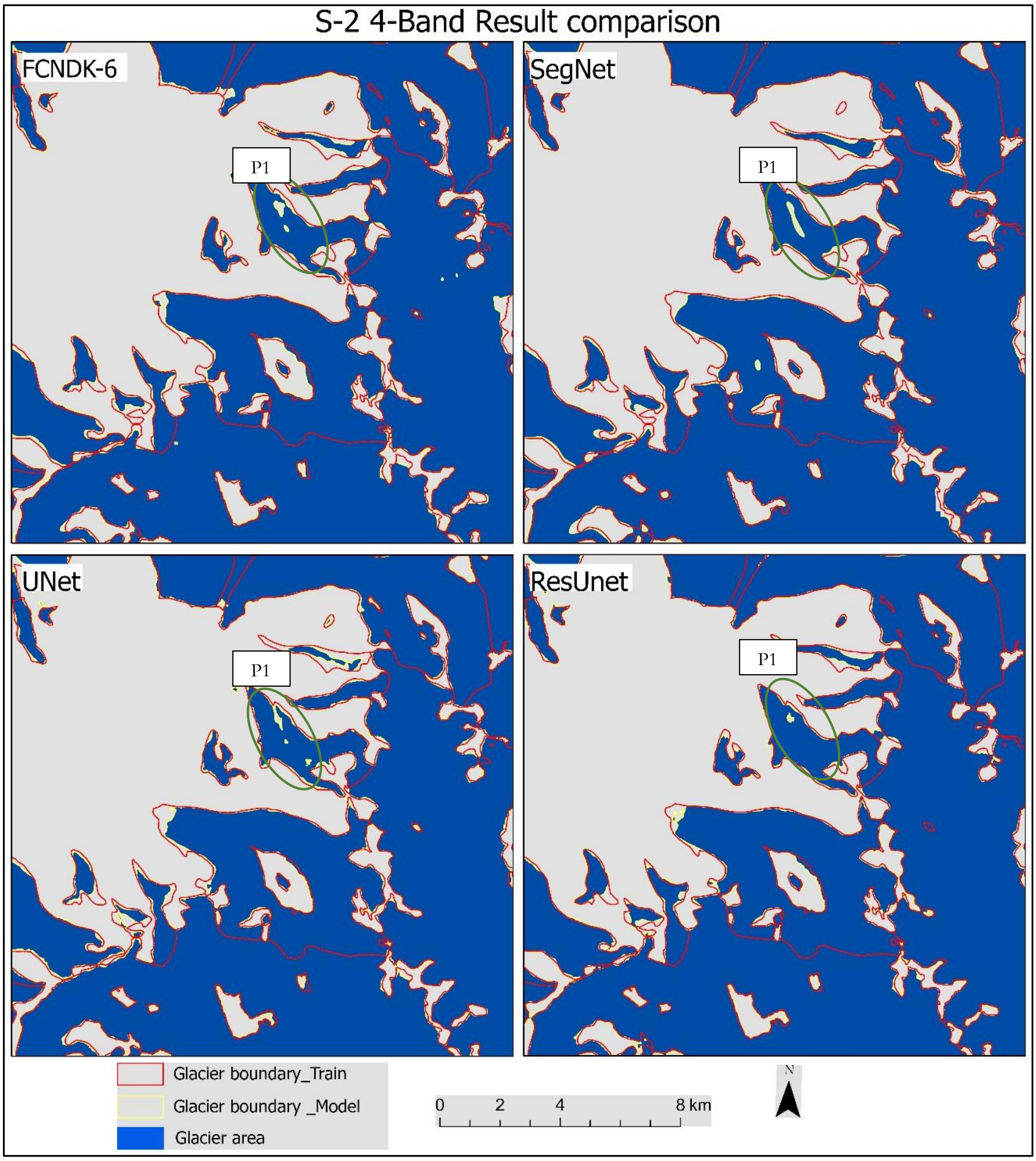

Figure 6.6: Sentinel-2 four-band results from all models; the images are the out of cross-entropy loss function a. is a result of FCNDK-6, b. shows the output of SegNet, c. is an output of UNet and d. is ResUnet output

6.2.2 Experiment with 12-band

In the twelve band experiment, we consider ultra-blue, blue, green, red, NIR, visible, and Infrared (VNIR), and Shortwave Infrared (SWIR) bands of sentinel-2. As the SWIR band has competitively lower reflectance, it is helpful while studying the glacier. When it comes to calculating the normalized snow index, we always consider the SWIR and green band. Therefore we included all bands of sentinel-2, which gives the surface reflectance. The twelve bands are used as an input channel in each network. All network in this experiment was calibrated with the pre-defined hyperparameter mentioned in section 6.2. The cumulative accuracy while considering the mean of all testing tiles is mentioned in Table *6.6*. The results show that the UNet cross-entropy gives the best performance compared to the other network.

Table 6.6: Result of Sentinel-2 12-band experiment

	FCN DK6		SegNet		UNet		ResUnet	
	Cross Entropy	BFL	Cross Entropy	BFL	Cross Entropy	BFL	Cross Entropy	BFL
Accuracy	0,9739	0,9765	0,9414	0,9729	0,9811	0,9788	0,9811	0,9795
Recall	0,8417	0,8339	0,7918	0,8171	0,8712	0,8099	0,8246	0,8137
Precision	0,9589	0,9622	0,9331	0,9581	0,9599	0,9662	0,9715	0,9577
F1	0,8797	0,8734	0,8473	0,8590	**0,9048**	0,8481	0,8646	0,8365

6.2.2.1 Result analysis of 4-band experiment

Figure *6.7*is the segmentation output of test tile-13(shown in Figure *6.5*). Major differences in segmentation for the bigger area of glacier and non-glacier regions are not observed. Whereas, small regions such as points p1 and p2 are not precisely segmented as glacier boundaries. Pont p2 in the SegNet has been segmented as a non-glacier area instead of a Glacier area, whereas the other networks precisely demarcated point p2 as a glacier area.

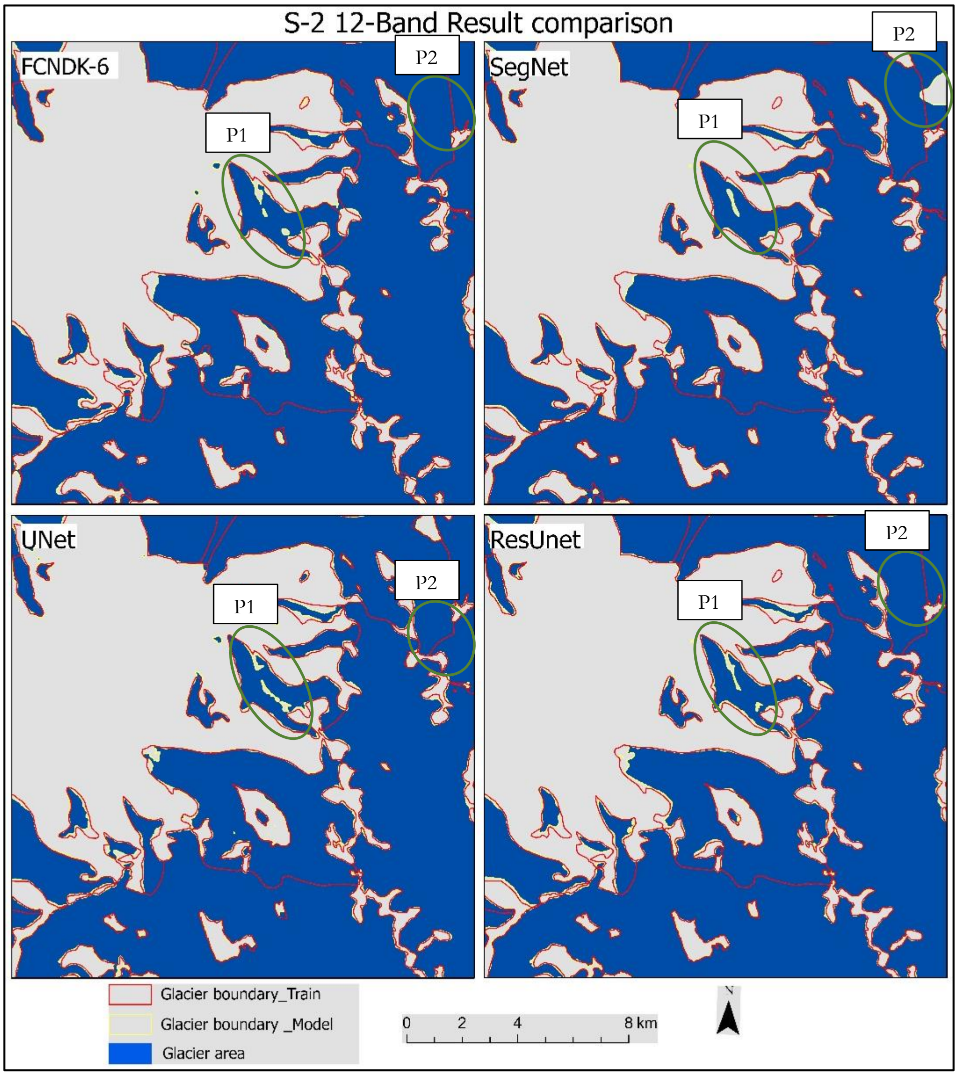

Figure 6.7: Sentinel-2 twelve band results from all models; the visuals are the out from cross-entropy loss function a. is the result of FCNDK-6, b. shows the output of SegNet, c. is an output of UNet and d. is ResUnet output

6.3 Fusion experiment

In the fusion experiment, we did the data fusion of Sentinel-1 and Sentinel-2. We applied the pre-network fusion techniques. We set up the Fusion experiment in four different setups. Fist with seven bands, the second experiment is with the ten bands, the third with fifteen bands, and the fourth experiment is an 18-band experiment. This band combination is based on experiments and its results from sections 6.2 and 6.3. These four setups were further run on different deep learning networks called FCN-DK6, SegNet, UNet, and ResUnet. We defined common hyperparameters based on experiments conducted at the beginning of this chapter in these all setups. We considered that all networks must use learning rate hyperparameters- 10^{-4}, patch size – 128, batch size -16, and the number of epochs -300. We also set the early stopping on validation loss for epochs parameter with patience thirty, but we noticed none of the network run trained till 300 epochs.

6.3.1 Experiment with 7-band

In the seven-band experiment, we used three bands of sentinel-1 and four sentinel-2. We combined the 3-band experiment of sentinel-1 and the 4-band experiment of sentinel-2. Here we considered C11, C22, and C11 real of the covariance matrix and Blue, green, red, and NIR of the optical sensor. We performed this experiment with all networks five times to have a significant result. The results from each network are mentioned in Table 6.7. UNet with cross-entropy loss produced the best result among all the networks.

Table 6.7: Result of fusion data of 7-band experiment

	FCN DK6		SegNet		UNet		ResUnet	
	Cross Entropy	BFL	Cross Entropy	BFL	Cross Entropy	BFL	Cross Entropy	BFL
Accuracy	0,9734	0,9773	0,9676	0,9125	0,9804	0,9752	0,9801	0,9780
Recall	0,8418	0,8389	0,7625	0,5921	0,8707	0,8149	0,8620	0,8512
Precision	0,9565	0,9331	0,9691	0,9636	0,9641	0,9696	0,9670	0,9705
F1	0,8859	0,8707	0,8227	0,7042	**0,9023**	0,8645	0,8898	0,8839

6.3.2 Experiment with 10-band

In the 10-band setup, we included all six bands from the sentinel-1 6-band experiment and combined them with all bands from the 4-band sentinel-2 experiment. In this experiment, six of ten input channels are from the SAR, and four are from the optical sensor. The FCN-DK6 with binary loss function showed the best result. The results from all network for the 10-band experiment is shown in Table 6.8

Table 6.8: Result of 10-band experiment from image fusion

	FCN DK6		SegNet		UNet		ResUnet	
	Cross Entropy	BFL	Cross Entropy	BFL	Cross Entropy	BFL	Cross Entropy	BFL
Accuracy	0,9695	0,9693	0,9609	0,9304	0,9586	0,9553	0,9472	0,9436
Recall	0,8022	0,8271	0,8433	0,7873	0,7840	0,7861	0,7195	0,7421
Precision	0,9375	0,9203	0,8128	0,7197	0,9043	0,9608	0,9073	0,9088
F1	0,8395	**0,8601**	0,8187	0,7303	0,8203	0,8362	0,7772	0,7896

6.3.3 Experiment with 15-band

15-band experiment is the combination of twelve band sentinel-2 and three-band from sentinel-1. After getting the best result from the SAR experiment, which is from 3-band-experiment whereas the Optical experiment is a 12-band experiment, we include this combination because the best performing results in the standalone method. Interestingly, in this experiment, we found that apart from SegNet, all network was stable. The ResUnet with binary loss function provided the best result. We also observed that the BFL loss function gave a better result than the cross-entropy loss. The overall mean accuracy matrix from all test tiles is mentioned in Table *6.9*.

Table 6.9: Result of fusion data of 10-band experiment

	FCN DK6		SegNet		UNet		ResUnet	
	Cross Entropy	BFL	Cross Entropy	BFL	Cross Entropy	BFL	Cross Entropy	BFL
Accuracy	0,9778	0,9783	0,8659	0,8974	0,9802	0,9782	0,9810	0,9825
Recall	0,8313	0,8527	0,5792	0,6130	0,8463	0,8051	0,8279	0,8559
Precision	0,9591	0,9536	0,9470	0,8786	0,9711	0,9710	0,9666	0,9792
F1	0,8756	0,8894	0,6999	0,7063	**0,8841**	0,8595	0,8715	0,8936

6.3.4 Experiment with 18- a band

In the setup of the 18-band experiment, we combined all produced bands from sentinel-1 and sentinel-2. The 12-band experiment of sentinel-2 provided the best result, so we included all sentinel-2 bands. With the results, the UNet with cross-entropy performed best among all networks. The results are mentioned in Table *6.10*.

Table 6.10: Result of fusion data of 18-band experiment

	FCN DK6		SegNet		UNet		ResUnet	
	Cross Entropy	BFL	Cross Entropy	BFL	Cross Entropy	BFL	Cross Entropy	BFL
Accuracy	0,9759	0,9741	0,6627	0,6570	0,9711	0,9715	0,9652	0,9663
Recall	0,8661	0,8297	0,8313	0,8515	0,8959	0,8936	0,7787	0,7979
Precision	0,9366	0,9452	0,4606	0,4562	0,9580	0,9321	0,9672	0,9450
F1	0,8868	0,8592	0,5361	0,5354	**0,9177**	0,8991	0,8298	0,8364

6.3.4.1 Result analysis from fusion network

We observed that the performance of the 18-band experiment has a better f1 score among different band combinations of the fusion data. Parallelly, we observed that the 7-band experiment has stable performance and achieves a high f1 score after the 18-band experiment. In Figure *6.8*, we analysed the result of test tile 18 from two different perspectives. Here we considered one of the lowest f1 scores and the efficient result from the 18-band experiment. We can observe here that the least performed network produces inconsistent results by over-estimation of glacier area. This network also included the water(highlighted with point p1) and some shadowed mountains (highlighted with point p2) as a glacier.

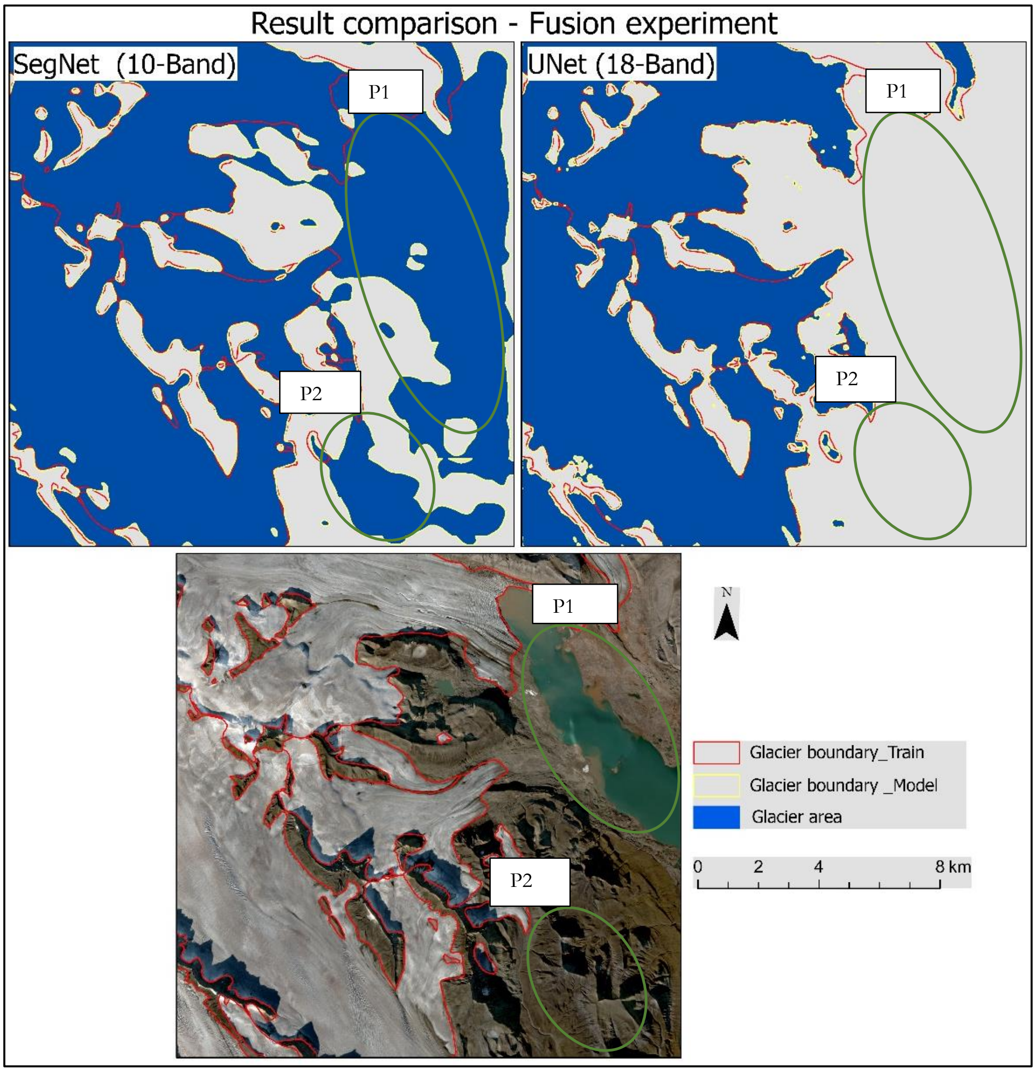

Figure 6.8: Comparison of the least performed and high-performing networks with fusion data. a. is the result of FCNDK-6, b. shows the output of SegNet, c. is an output of UNet and d. is ResUnet output.

6.4 Results comparison

In Table *6.11*, we present the best-performed networks from different datasets. We observed that 3-band experiments from Sentinel-1 SAR datasets, 12-band from Sentinel-2 Optical datasets, and 18-band from fusion datasets gave better results with standalone and fusion networks, while the UNet performance was stable throughout the experiments. The accuracy result shown in Table *6.11* is the mean of all test tiles of its network.

Table 6.11: Best results with different datasets and among all networks

	UNet S1 (3-band)	UNet S2 (12-band)	UNet Fusion (18-band)
Accuracy	0,9365	0,9811	0,9711
Recall	0,7631	0,8712	0,8959
Precision	0,7515	0,9599	0,9580
F1	0,7507	0,9048	**0,9177**

6.4.1 SAR verses Optical

Each experiment with SAR data has less f1 score compared to the experiments with optical data. The f1 score of S1 based model is 0.7507, which is more than 75%, whereas the optical achieved more than 90% with an f1 score of 0.9048. The f1 score differs between both the Model I by almost 15%. The highest accuracy of SAR and Optical different band experiments is shown in Figure *6.9*, where the performance of the different band experiments varies.

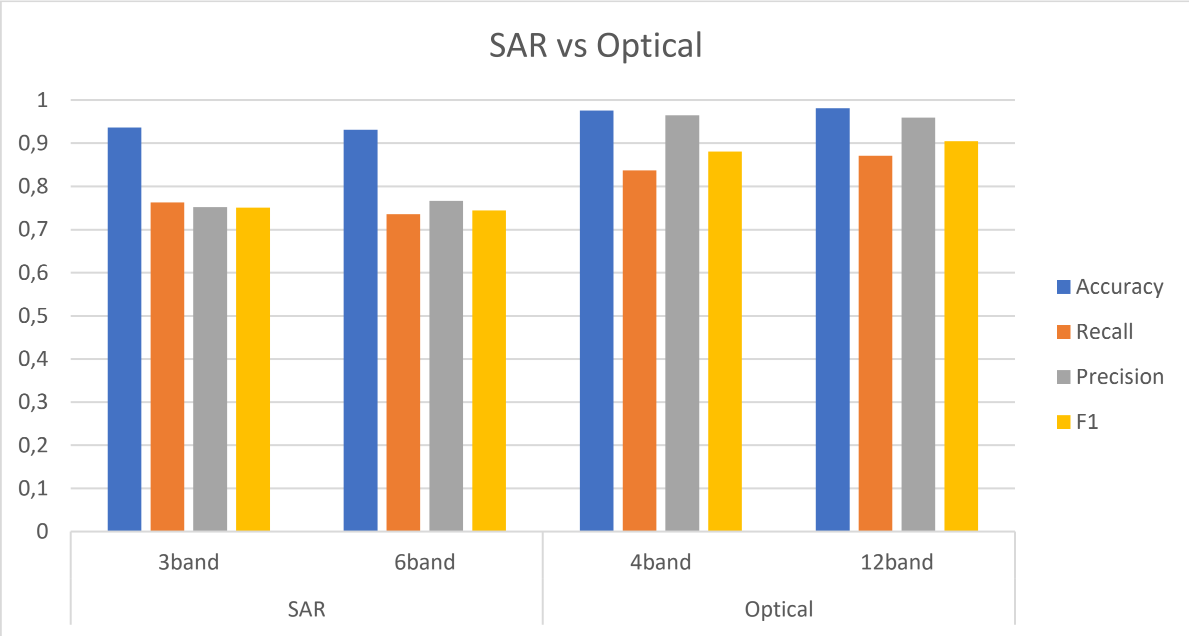

Figure 6.9: SAR vs. Optical, different band experiments accuracy

6.4.2 SAR versus Fusion

The accuracy of the Sentinel-1 SAR-based model is 75%, whereas the fusion achieved 91% of accuracy. The different band combinations experiments result is shown in Figure *6.10*. The performance of SAR data is comparatively lower accuracy in both 3-band and 6-band experiments.

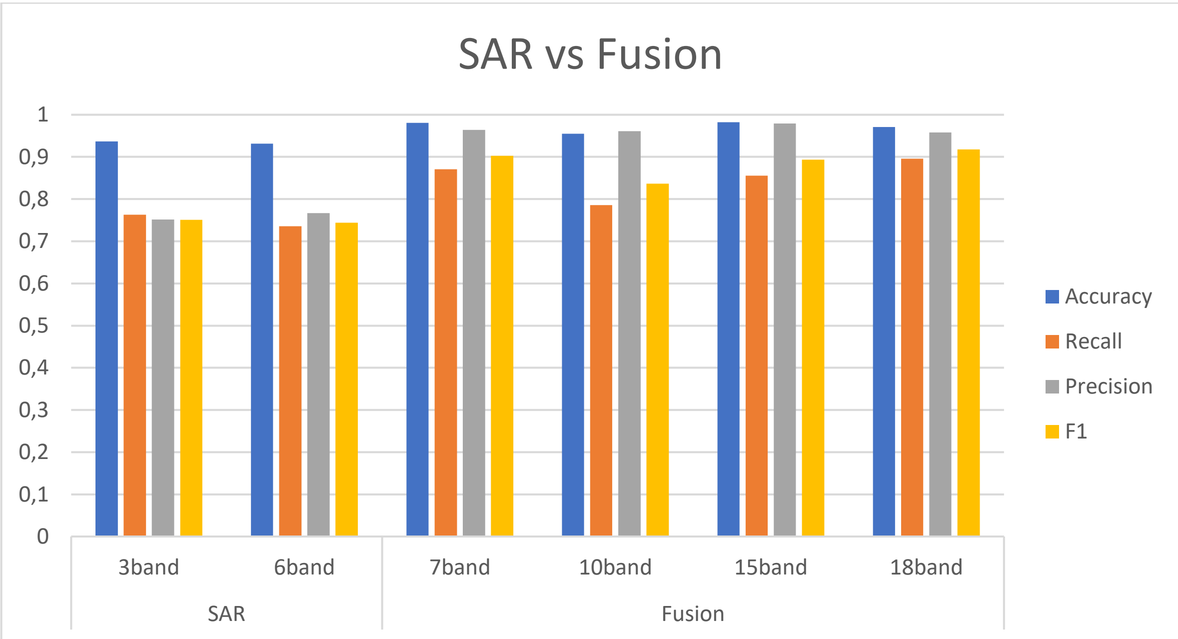

Figure 6.10: SAR vs. Fusion with different band experiment's accuracy

6.4.3 Optical versus Fusion

Figure *6.11* shows that the highest accuracy was achieved from different experiments using the optical and the fusion datasets. Accuracy as F1 score for glacier boundary output shows that the 18-band fusion experiment has comparatively highest accuracy than 4-band and 12-band optical experiment.

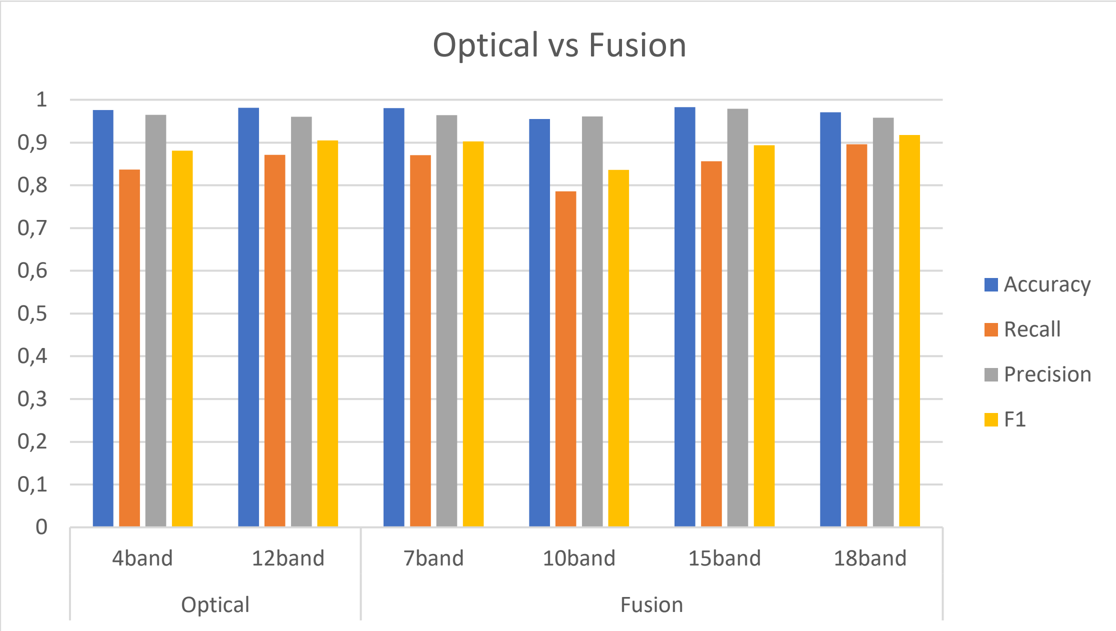

Figure 6.11: Optical vs. Fusion using different band experiments accuracy

6.4.4 SAR Optical and fusion

Figure *6.12* shows that the best performance experiment is with 18-band of fusion datasets, whereas the least accuracy is with 6-band SAR data experiment. We can observe here that the combing sentinel-1 and sentinel-2 data increased the f1 score.

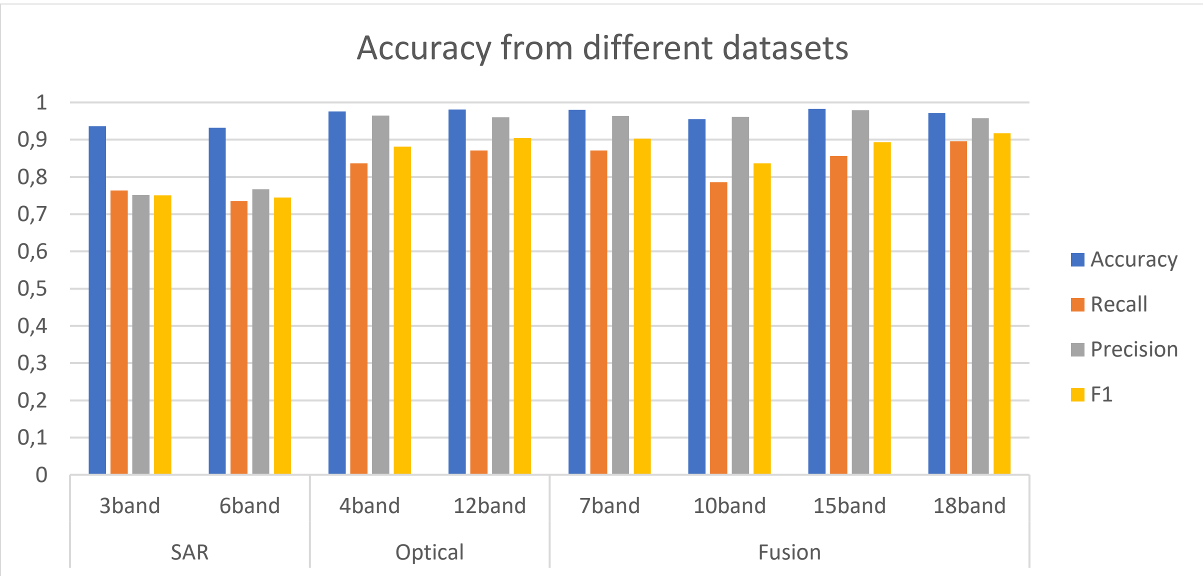

Figure 6.12: SAR, Optical, and Fusion different band experiments accuracy

In Figure *6.13*, we presented the highlights of the differences in the results from all three datasets. In this figure, different colours represent the glacier boundary delineated by different datasets, the yellow line represents the output from the sentinel-1 datasets, the pink is the glacier boundary from Sentinel-2, and green is the output of fusion datasets.

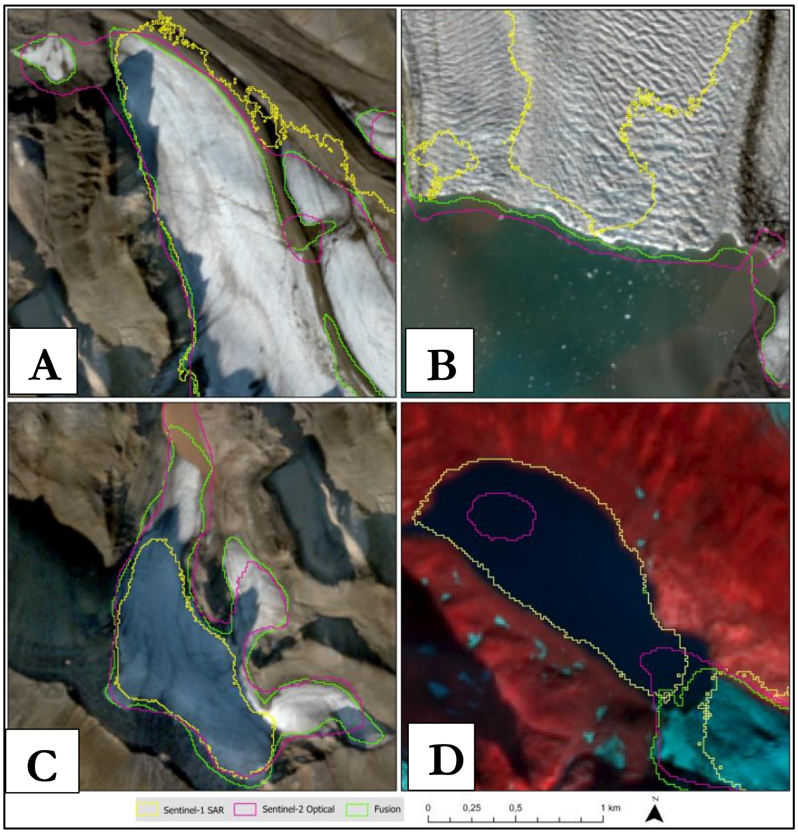

Figure 6.13: Glacier boundary from SAR, Optical, and Fusion experiments

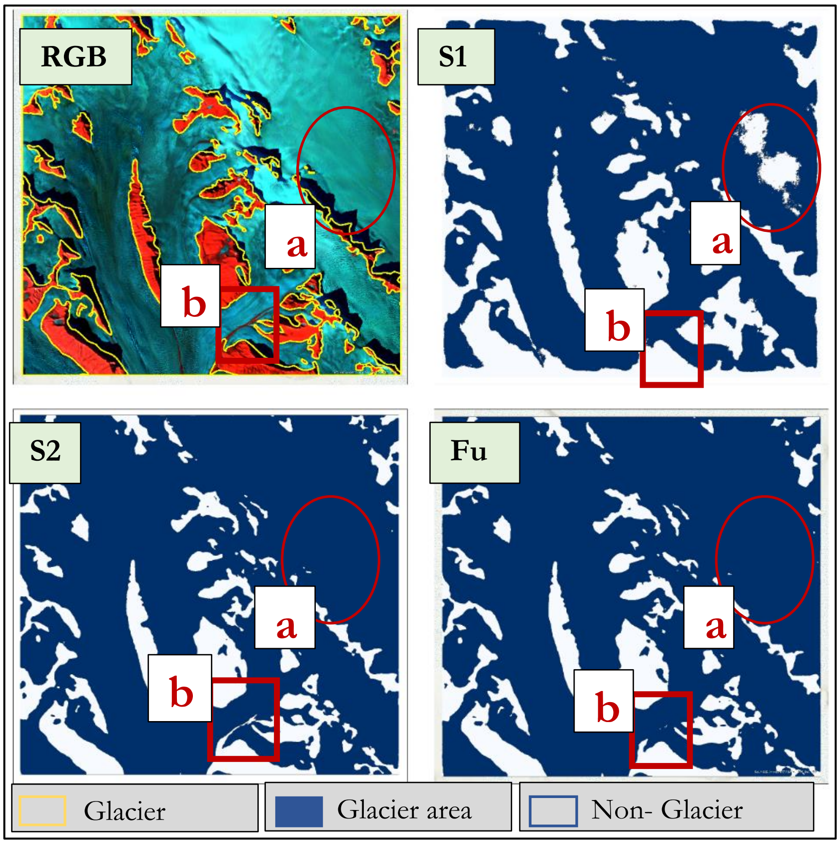

Figure 6.14: Highlighted the points and shows the qualitative variation of results from different datasets.

7 DISCUSSION

This chapter is the discussion of the results of all adopted methods during this research. We parted this chapter into different sections. In the first section of this chapter, we discussed the evaluation methods and compared with existing research, In second section, we describe the accuracies of our adopted methods, followed by the highlights of the qualitative outputs. Later, we discuss the values of our output to de-intensify the wickedness. At the end, we emphasize the limitation of this research.

7.1 Evaluation of the Methods

After applying multiple combinations of input data channels in different networks to extract the glacier extent, we found some reliability in the methods. UNet provided the stable and comparative best glacier extent in our findings out of all applied deep learning networks. While with different datasets, we found that combining the optical and SAR increases the performance and enhances the glacier extent demarcation.

Regarding the result compression section 6.4, we found methods worked significantly with Sentinel-1 and Sentinel-2 datasets, but there is some positive and negative aspect in both cases. Although the results with S-1 were not able to predict glacier extend precisely with respect to S-2 data which will need more manual corrections. SAR data has the problem of speckles, and it requires a more refined way while removing the speckles (Mullissa et al., 2017). At the very beginning of the experiment, we also faced a problem with the performance of the S-1-based model and gave poor results, but later after changing the speckle filter techniques, we managed to improve our accuracies. While utilizing the scattering properties in our network, we also had limitations of dual-polarization data, Shi and Dozier, (1993) showed the richness while using full pol data and its effect on accuracies.

Our best-performed experiment, which is 18-band with UNet network, which is also novel in this research for glacier extent mapping, accounting for the research of Alifu et al., (2020) and Fernandez-Beltran et al., (2018). Although the consistency with the UNet was since our first experiment, which also continued with the 18 band experiment. Combining the S-1 and S-2 data increases the accuracy comparatively with standalone use of the data. In another experiment with fusion data, we also observed that the 7-band experiment also has (S-1 3band and S2 4band standalone) stable performance comparatively and achieves consistent glacier extent after the 18-band experiment. So, It is important here to mark that either S-1 or S-2 is not enough to map glacier extent. We also found that the best-performed network's glacier extent still needs correction in some regions, such as misclassification between the shadow cover area or the confusion between fresh snow in the non-glacier area and the glacier area. Some patches of the snow away from the glacier region are also classified as the glacier area and demarcated as separate glacier polygons. Although there is a need for manual correction after the network, it decreases the manpower and the lesser the time from mapping glacier extent manually.

Since the frequency of glacier extent mapping and the update of the existing database, such as RGI or GLIMS, is in decades. The results show a good potential to expand the use of fusion networks and adopt the methods. Xie et al., (2020) implemented DL to map the debris-covered glacier using Landsat images (optical) and managed to get significant results for a small region, whereas our optical data-based model extends in the spatial domain with considerable accuracies. We extended with respect to data and included the SAR and data fusion techniques.

7.2 Accuracies of the methods

We extracted the glacier and non-glacier area using almost every experiment as per our primary goal of glacier extent extraction. But there was always variation in the results. The extent from different models does not always overlay with the real extent of the glacier. So check the variation and shifts we applied evaluation matrix, mentioned in section 5.6. The matrix we used is based on the F1 score of the models. There were variations in the F1 score of the different models and the different experiments. Such as, the results we got during the experiments using the Sentinel-1 data were not accurate as of the output from the

Sentinel-2 data. Parallelly we also found that even all models have not had the same F1 score from the same data because of the variation in their architecture. The different networks allow different ways while highlighting the spatial-contextual and the textural features.

In the case of the results from the Sentinel-1 experiments, our 3-band experiments provided comparatively higher F1 values, but at the same time, SegNet has almost 20% less accurate prediction value than the UNet model. After the multiple attempts of the model run, we observed that, in the case of Sentinel-1 data, FCNDK and the UNet have stable output, although the accuracy from the UNet was more consistent and higher F1 score.

Sentinel-2-based model performance was higher than the Sentinel-1-based model. As we mentioned in section 6.2, we run all networks in two different input setups; first, we only used 10m Blue, Green, Red, and NIR bands and managed to achieve an F1 score of 0.88. Later we included SWIR and other NIR bands and used twelve bands as input. In the case of the 12-band, we observed that the same UNet model (used for the 4-band experiment) increased the accuracy by 2% and managed to have an F1 value of 0.90.

In our novel experiment, we fused the Sentinel-1 and sentinel-2 datasets and checked their influence on the results. We realized that fusing the data from these two optical and SAR satellites quite an improvement in F1 value. We also observed that the same model with a standalone method gave better results with fusion data. For example, FCNDK with Sentinel-1 3-band experiment has F1 score 0.73, and Sentinel-2 4-band experiment has 0.83, and when we fused same three bands from S1, and four bands from S2, and performed 7-band fusion experiment we achieved 0.88 of F1 score, but this was not always the case. In our final attempt at the experiment, we conclude that the 18-band fusion experiments provided the best result, as mentioned in table section 6.4.

7.3 Qualitative highlights

We also checked our results manually and analysed the quality by overlapping the output of one model with another's. Figure 6.13 highlighted the three different extend of different datasets from the best-performed model. We presented four different scenarios in Figure *6.13*, A)Two different Glaciers partially separated, B) Glacier with irregular shapes connecting to the fjord (waster), C) Single Glacier mostly covered with a shadow, and the last D) the mountain lake meeting to the glacier. Here we found the variation of the results when the glacier meets the water (in Figure *6.13* B and D). The poorly performed model had confusion, to some extent, between the glacier area surrounded by water. On the other hand, there is also confusion when separating glaciers from other glaciers. There are also uncertainties while mapping the extent of the shadowed region. We are also highlighting another example in Figure *6.14* (RGB shows the band 8-4-3 of sentinel-2 data, S1 represents Sentinel-1 based model output, S2 is Sentinel-2 output, and Fu shows the output from the data fusion model). Here we can observe that in the middle of the glacier area at point '**a**', the best-performed Model with SAR data has uncertainty while defining the extent and included potion of glacier area as a non-glacier area, whereas the model used optical and fused data perfectly working. At point-b of figure 6-14, we noticed that model that used optical datasets has some confusion in the dirty portion of the Glacier (Glacier consisting of dark objects). Although this model has higher accuracy, it is making contour in dirty glacier part, while the less accurate Model (S1) is able to predict correctly (We didn't investigate the reason behind it, but probably because SAR has a higher wavelength and penetration capacity), and it is also predicted correctly in the fusion-based model. In the final observation, we conclude that sometimes the standalone methods are not able to predict specific regions, whereas combining both datasets in one Model (Fusion model) is able to map correctly.

7.4 De-intensification of wickedness

The role of the accurate glacier database is important and needed during numerous research from different sectors, Such as climatologists use glacier data in their models for precise future climate prediction, meteorologist uses it as one parameter for weather forecast, hydrologist uses it for mass balance or daily discharge or the flow, most importantly glaciologist uses it in their every research, etc. To have a robust model for precisely glacier extent mapping, our current research might make a major contribution to building and updating the glacier database and a small direct and indirect contribution to all studies and research that will use the database. As we elaborated on the complexity of the data gap problem of the glacier in 1.2, this research will lead to fulfilling having a robust method gap and increasing the resolutions of the data. We also found and discussed in section 1.2 the continuous decline in earth's climate quality; having this robust model will help continuously monitor glacier health, which highly influence the climate (Bosson et al., 2019).

7.5 Limitations

During this study, our major limitation was the hardware inaccessibility, and these deep learning models use a huge amount of GPU memory which was limited for my personal laptop. These deep learning libraries also depend on the coding feasibility and the processing time, as these models use multiple convolutional layers. So it consumes and drains processing power during its run. Our research was limited to a single timeframe and ran our model with a single image.

8 CONCLUSION AND RECOMMENDATIONS

8.1 Conclusion

The primary objective of this research was to use deep learning methods to map the glacier extent for Svalbard, and Jostedalsbreen, Norway region. This research implemented and evaluated the different deep learning networks to map the glacier extent using freely available opensource Sentinel datasets. We applied all these methods to the Sentinel-1 SAR and Sentinel-2 optical datasets separately, and later we introduced the SAR and optical data fusion into the networks.

To conclude my research, we answered our research question mentioned in section 1.6.

1. What is the overall accuracy that can be achieved when separating glacier and non-glacier extent using standalone Sentinel-1 and Sentinel-2 imageries?

We tried a series of experiments with different band combinations and applied multiple runs while tunning the models. We run our Model with Sentinel-1 and Sentinel-2 data separately in the standalone method. The final results of all combinations from S-1 and S-2 are mentioned in sections 6.2 and 6.3, respectively. From sentinel-1, we achieved the highest F1 score of 0.75 using three bands with the help of the UNet model. Whereas experimenting with the Sentinel-2 optical dataset, we managed to increase the F1 score. We obtained F1 of 0.90 as the highest with S2 datasets while using twelve bands as an input in the UNet model.

2. What is the overall accuracy that can be achieved after fusing Optical and SAR data to map the glacier extent?

Data fusion of Sentinel-1 SAR and Sentinel-2 optical was executed in different sequences. First, we combined the three different channels from SAR data and four different input channels from optical, and with these combinations, we achieved an F1 score of 0.86. We later also tried the combination of ten and fifteen bands, the accuracy in detailed mention in section 6.4. We continued our experiment until the all-band combination was used in the standalone method and achieved the highest accuracy. With eighteen band combinations, we received the F1 score of 0.91 and observed balance precession and recall in UNet. So overall, we have the highest accuracies from the UNet 18-band experiment.

3. Which band combinations of Sentinel-1 and Sentinel-2 efficiently improve the glacier area mapping?

In chapter-6, we elaborated intensively on the band combinations and defined their reason. We started our model with the three-channel of Sentinel-1 mentioned in section 5.2.1 of the covariance matrix. Later, we included three more channels and combinedly run the model to check the improvement, but there was no improvement. In the next step, we started our experiment with Sentinel-2 NIR and RGB bands of 10m. The model was better predicted the glacier extent and able to classify glacier and non-glacier areas comparatively more accurately than Sentinel-1. After that, we also included SWIR and other NIR bands because the literature suggests that the SWIR bands better performed with glacier studies. Including SWIR and other NIR bands of Sentinel-2 optical data in the model, we combined twelve input channels and achieved higher accuracy than the optical four band.

4. How can the different combinations of SAR data help to map glacier extent?

Our research used Sentinel-1 SAR data of VV and VH polarimetric channels. We explore the use of phase and amplitude of this polarization. We found that the single image phase information was not useful during the research and introduced noises to our networks. (explained in section 5.2.1 'Exploration of phase information). Later we created a matrix(mentioned in section 5.2.1 equation 5.2), and from the out of this matrix, we created three different channels (we called them c11, c22, and c12real). These three combinations were further used as three inputs in networks and worked properly. We also generated bands while differentiating on the basis of the scattering mechanism of SAR data (explained in section 5.2.1 'decomposition'), but including these bands did not improve the model accuracies in this research. So we conclude that the three-channel (C11, C22, and C12real) generated from VV and VH polarimetric was better in performance while using the Sentinel-1 SAR data.

8.2 Recommendation

In the future, this work can be extended while exploring the opportunity with SAR datasets. Although we managed to map the glacier and extend it using SAR data, the accuracy was comparatively lower than the optical data. We can explore the addition of backscattered properties and specifically define the backscatter values for the glacier studies. This study was also restricted to dual-polarization data, including fully polarimetric data might be interesting research. There is also an exploration possibility of temporal SAR data such as interferometric features, multi images phase information, etc. We also faced problems of speckling in SAR data and used de-speckling methods outside the network to resolve them. So we can further introduce a deep learning model which can able to solve this speckle problem inside the network and reduce the extra burden of pre-processing.

9 REFERENCES

Albawi, S., Mohammed, T.A., Al-Zawi, S., 2017. Understanding of a convolutional neural network, in: 2017 International Conference on Engineering and Technology (ICET). pp. 1–6. https://doi.org/10.1109/ICEngTechnol.2017.8308186

Albright, T.P., Painter, T.H., Roberts, D.A., Shi, J., 1998. Classification of surface types using SIR-C/X-SAR, Mount Everest Area, Tibet. Journal of Geophysical Research E: Planets 103, 25823–25837. https://doi.org/10.1029/98je01893

Alifu, H., Vuillaume, J.F., Johnson, B.A., Hirabayashi, Y., 2020. Machine-learning classification of debris-covered glaciers using a combination of Sentinel-1/-2 (SAR/optical), Landsat 8 (thermal) and digital elevation data. Geomorphology 369, 107365. https://doi.org/10.1016/j.geomorph.2020.107365

Andreassen, L.M., Elvehøy, H., Kjøllmoen, B., 2002. Using aerial photography to study glacier changes in Norway. Annals of Glaciology 34, 343–348. https://doi.org/DOI: 10.3189/172756402781817626

Andreassen, L.M., Winsvold, S.H., Paul, F., Hausberg, J.E., 2012. Inventory of Norwegian Glaciers, NVE Rapport.

Arlov, T.B., 2006. The Discovery and Early Exploitation of Svalbard. Some Historiographical Notes. http://dx.doi.org/10.1080/08003830510020343 22, 3–19. https://doi.org/10.1080/08003830510020343

Badrinarayanan, V., Kendall, A., Cipolla, R., 2017. Segnet: A deep convolutional encoder-decoder architecture for image segmentation. IEEE Trans Pattern Anal Mach Intell 39, 2481–2495.

Barzycka, B., Grabiec, M., Błaszczyk, M., Ignatiuk, D., Laska, M., Hagen, J.O., Jania, J., 2020. Changes of glacier facies on Hornsund glaciers (Svalbard) during the decade 2007–2017. Remote Sensing of Environment 251, 112060. https://doi.org/10.1016/j.rse.2020.112060

Baumhoer, C.A., Dietz, A.J., Kneisel, C., Kuenzer, C., 2019. Automated extraction of antarctic glacier and ice shelf fronts from Sentinel-1 imagery using deep learning. Remote Sensing 11, 1–22. https://doi.org/10.3390/rs11212529

Benson, C.S., 1959. Physical investigations on the snow and firn of northwest Greenland 1952, 1953, and 1954. US Army Snow Ice and Permafrost Research Establishment, Corps of Engineers.

Bhardwaj, A., Joshi, P.K., Snehmani, Sam, L., Singh, M.K., Singh, S., Kumar, R., 2015. Applicability of Landsat 8 data for characterizing glacier facies and supraglacial debris. International Journal of Applied Earth Observation and Geoinformation 38, 51–64. https://doi.org/https://doi.org/10.1016/j.jag.2014.12.011

Bhardwaj, A., Sam, L., Akanksha, Martín-Torres, F.J., Kumar, R., 2016. UAVs as remote sensing platform in glaciology: Present applications and future prospects. Remote Sensing of Environment 175, 196–204. https://doi.org/https://doi.org/10.1016/j.rse.2015.12.029

Bishop, M.P., Kargel, J.S., Kieffer, H.H., MacKinnon, D.J., Raup, B.H., Shroder, J., 2000. Remote-sensing science and technology for studying glacier processes in high Asia. Annals of Glaciology 31, 164–170. https://doi.org/10.3189/172756400781820147

Bolch, T., Buchroithner, M., Pieczonka, T., Kunert, A., 2008. Planimetric and volumetric glacier changes in the Khumbu Himal, Nepal, since 1962 using Corona, Landsat TM and ASTER data. Journal of Glaciology 54, 592–600. https://doi.org/10.3189/002214308786570782

Bolch, T., Pieczonka, T., Benn, D.I., 2011. Multi-decadal mass loss of glaciers in the Everest area (Nepal Himalaya) derived from stereo imagery. Cryosphere 5, 349–358. https://doi.org/10.5194/tc-5-349-2011

Bosson, J. -B., Huss, M., Osipova, E., 2019. Disappearing World Heritage Glaciers as a Keystone of Nature Conservation in a Changing Climate. Earth's Future 7, 469–479. https://doi.org/10.1029/2018EF001139

Brown, I.A., 2012. Synthetic Aperture Radar Measurements of a Retreating Firn Line on a Temperate Icecap. IEEE Journal of Selected Topics in Applied Earth Observations and Remote Sensing 5, 153–160. https://doi.org/10.1109/JSTARS.2011.2167601

Brown, J.A., 2003. Radar facies on the West Greenland ice sheet : Comparison with A VHRR albedo data 367–372.

Chen, F., 2021. Comparing Methods for Segmenting Supra-Glacial Lakes and Surface Features in the Mount Everest Region of the Himalayas Using Chinese GaoFen-3 SAR Images. Remote Sensing 13, 2429. https://doi.org/10.3390/rs13132429

Chicco, D., Jurman, G., 2020. The advantages of the Matthews correlation coefficient (MCC) over F1 score and accuracy in binary classification evaluation. BMC Genomics 21, 6. https://doi.org/10.1186/s12864-019-6413-7

Cloude, S.R., Pottier, E., 1997. An entropy based classification scheme for land applications of polarimetric SAR. IEEE Transactions on Geoscience and Remote Sensing 35, 68–78. https://doi.org/10.1109/36.551935

Cogley, J.G., Arendt, A.A., Bauder, A., Braithwaite, R.J., Hock, R., Jansson, P., Kaser, G., Moller, M., Nicholson, L., Rasmussen, L.A., 2010. Glossary of glacier mass balance and related terms.

Dargan, S., Kumar, M., Ayyagari, M.R., Kumar, G., 2020. A Survey of Deep Learning and Its Applications: A New Paradigm to Machine Learning. Archives of Computational Methods in Engineering 27, 1071–1092. https://doi.org/10.1007/s11831-019-09344-w

de Angelis, H., Rau, F., Skvarca, P., 2007. Snow zonation on Hielo Patagónico Sur, Southern Patagonia, derived from Landsat 5 TM data. Global and Planetary Change 59, 149–158. https://doi.org/10.1016/j.gloplacha.2006.11.032

Dirscherl, M., Dietz, A.J., Kneisel, C., Kuenzer, C., 2021. A novel method for automated supraglacial lake mapping in antarctica using sentinel-1 sar imagery and deep learning. Remote Sensing 13, 1–27. https://doi.org/10.3390/rs13020197

Echelmeyer, K., Harrison, W.D., Clarke, T.S., Benson, C., 1992. Surficial glaciology of Jakobshavns Isbrae, west Greenland: part II. Ablation, accumulation and temperature. Journal of Glaciology 38, 169–181. https://doi.org/10.1017/S0022143000009709

Farnsworth, W.R., Allaart, L., Ingólfsson, Ó., Alexanderson, H., Forwick, M., Noormets, R., Retelle, M., Schomacker, A., 2020. Holocene glacial history of Svalbard: Status, perspectives and challenges. Earth-Science Reviews 208, 103249. https://doi.org/10.1016/J.EARSCIREV.2020.103249

Fernandez-Beltran, R., Haut, J.M., Paoletti, M.E., Plaza, J., Plaza, A., Pla, F., 2018. Multimodal probabilistic latent semantic analysis for Sentinel-1 and Sentinel-2 image fusion. IEEE Geoscience and Remote Sensing Letters 15, 1347–1351. https://doi.org/10.1109/LGRS.2018.2843886

Gore, A., Mani, S., Hari, H.R., Shekhar, C., Ganju, A., 2019. Glacier surface characteristics derivation and monitoring using Hyperspectral datasets: a case study of Gepang Gath glacier, Western Himalaya. Geocarto International 34, 23–42. https://doi.org/10.1080/10106049.2017.1357766

Gupta, R.P., Haritashya, U.K., Singh, P., 2005. Mapping dry/wet snow cover in the Indian Himalayas using IRS multispectral imagery. Remote Sensing of Environment 97, 458–469. https://doi.org/10.1016/j.rse.2005.05.010

Hall, D.K., Riggs, G.A., 2010. Normalized-difference snow index (NDSI).

Hall, D.K., Riggs, G.A., Salomonson, V. v, 1995. Development of methods for mapping global snow cover using moderate resolution imaging spectroradiometer data. Remote Sensing of Environment 54, 127–140. https://doi.org/https://doi.org/10.1016/0034-4257(95)00137-P

Hartmann, A., Davari, A., Seehaus, T., Braun, M., Maier, A., Christlein, V., 2021. Bayesian U-Net for Segmenting Glaciers in SAR Imagery 1–4.

Heiskanen, J., Kajuutti, K., Jackson, M., Elvehøy, H., Pellikka, P., 1993. Assessment of Glaciological Parameters Using Landsat Sat- Ellite Data in Svartisen , Northern Norway. EARSeL eProceedings.

Hollmann, R., Merchant, C.J., Saunders, R., Downy, C., Buchwitz, M., Cazenave, A., Chuvieco, E., Defourny, P., de Leeuw, G., Forsberg, R., Holzer-Popp, T., Paul, F., Sandven, S., Sathyendranath, S., van Roozendael, M., Wagner, W., 2013. The ESA Climate Change Initiative: Satellite Data Records for Essential Climate Variables. Bull Am Meteorol Soc 94, 1541–1552. https://doi.org/10.1175/BAMS-D-11-00254.1

Holzmann, M., Davari, A., Seehaus, T., Braun, M., Maier, A., Christlein, V., 2021. Glacier Calving Front Segmentation Using Attention U-Net 2–5.

Huang, L., Li, Z., Tian, B. sen, Chen, Q., Liu, J.L., Zhang, R., 2011. Classification and snow line detection for glacial areas using the polarimetric SAR image. Remote Sensing of Environment 115, 1721–1732. https://doi.org/10.1016/j.rse.2011.03.004

Hubbard, B., Glasser, N.F., 2005. Field techniques in glaciology and glacial geomorphology. John Wiley & Sons.

Huss, M., Hock, R., 2015. A new model for global glacier change and sea-level rise. Frontiers in Earth Science 3. https://doi.org/10.3389/feart.2015.00054

Jacobsen, D., Milner, A.M., Brown, L.E., Dangles, O., 2012. Biodiversity under threat in glacier-fed river systems. Nature Climate Change 2, 361–364. https://doi.org/10.1038/nclimate1435

Jawak, S.D., Wankhede, S.F., Luis, A.J., 2019. Explorative study on mapping surface facies of selected glaciers from chandra basin, Himalaya Using WorldView-2 Data. Remote Sensing 11. https://doi.org/10.3390/rs11101207

Jiancheng Shi, Dozier, J., 1995. Inferring snow wetness using C-band data from SIR-C's polarimetric synthetic aperture radar. IEEE Transactions on Geoscience and Remote Sensing 33, 905–914. https://doi.org/10.1109/36.406676

Joshi, M.D., Bolzan, J.F., Jezek, K.C., Merry, C.J., 1998. Classification of snow facies on the Greenland ice sheet using passive microwave and SAR imagery, in: IGARSS'98. Sensing and Managing the Environment. 1998 IEEE International Geoscience and Remote Sensing. Symposium Proceedings.(Cat. No. 98CH36174). IEEE, pp. 1852–1854.

Karen Simonyan∗ & Andrew Zisserman+, 2018. VERY DEEP CONVOLUTIONAL NETWORKS FOR LARGE-SCALE IMAGE RECOGNITION Karen. American Journal of Health-System Pharmacy 75, 398–406.

Khan, A.A., Jamil, A., Hussain, D., Taj, M., Jabeen, G., Malik, M.K., 2020. Machine-Learning Algorithms for Mapping Debris-Covered Glaciers: The Hunza Basin Case Study. IEEE Access 8, 12725–12734. https://doi.org/10.1109/ACCESS.2020.2965768

König, M., Winther, J.G., Isaksson, E., 2001. Measuring Snow and Glacier ice Properties from Satellite. Reviews of Geophysics 39, 1–27. https://doi.org/10.1029/1999RG000076

Kulkarni, A. v, Srinivasulu, J., Manjul, S.S., Mathur, P., 2002. Field based spectral reflectance studies to develop NDSI method for snow cover monitoring. Journal of the Indian Society of Remote Sensing 30, 73–80.

Kundu, S., Chakraborty, M., 2015. Delineation of glacial zones of Gangotri and other glaciers of Central Himalaya using RISAT-1 C-band dual-pol SAR. International Journal of Remote Sensing 36, 1529–1550. https://doi.org/10.1080/01431161.2015.1014972

Laute, K., Beylich, A.A., 2021. Recent Glacier Changes and Formation of New Proglacial Lakes at the Jostedalsbreen Ice Cap in Southwest Norway BT - Landscapes and Landforms of Norway, in: Beylich, A.A. (Ed.), . Springer International Publishing, Cham, pp. 71–95. https://doi.org/10.1007/978-3-030-52563-7_4

Laute, K., Beylich, A.A., 2020. The formation of new glacial lakes at the Jostedalsbreen ice cap in southwest Norway and their future implications, in: EGU General Assembly Conference Abstracts, EGU General Assembly Conference Abstracts. p. 5012.

LEE, J.S., GRUNES, M.R., KWOK, R., 1994. Classification of multi-look polarimetric SAR imagery based on complex Wishart distribution. International Journal of Remote Sensing 15, 2299–2311. https://doi.org/10.1080/01431169408954244

Liu, F., Jiao, L., Hou, B., Yang, S., 2016. POL-SAR Image Classification Based on Wishart DBN and Local Spatial Information. IEEE Transactions on Geoscience and Remote Sensing 54, 3292–3308. https://doi.org/10.1109/TGRS.2016.2514504

Long, J., Shelhamer, E., Darrell, T., 2015. Fully convolutional networks for semantic segmentation, in: 2015 IEEE Conference on Computer Vision and Pattern Recognition (CVPR). pp. 3431–3440. https://doi.org/10.1109/CVPR.2015.7298965

Marsland, S., 2011. Machine learning: an algorithmic perspective. Chapman and Hall/CRC.

Mohajerani, Y., Jeong, S., Scheuchl, B., Velicogna, I., Rignot, E., Milillo, P., 2021. Automatic delineation of glacier grounding lines in differential interferometric synthetic-aperture radar data using deep learning. Scientific Reports 11, 1–10. https://doi.org/10.1038/s41598-021-84309-3

Mohajerani, Y., Wood, M., Velicogna, I., Rignot, E., 2019. Detection of glacier calving margins with convolutional neural networks: A case study. Remote Sensing 11, 1–13. https://doi.org/10.3390/rs11010074

Müller, F., 1962. Zonation in the accumulation area of the glaciers of Axel Heiberg Island, NWT, Canada. Journal of Glaciology 4, 302–311.

Mullissa, A.G., Tolpekin, V., Stein, A., 2017. Scattering property based contextual PolSAR speckle filter. International Journal of Applied Earth Observation and Geoinformation 63, 78–89. https://doi.org/10.1016/j.jag.2017.07.011

Negrel, J., Gerland, S., Doulgeris, A.P., Lauknes, T.R., Rouyet, L., 2018. On the potential of hand-held GPS tracking of fjord ice features for remote-sensing validation. Annals of Glaciology 59, 173–180. https://doi.org/DOI: 10.1017/aog.2017.35

Nielsen, A.A., Canty, M.J., Skriver, H., Conradsen, K., 2017. Change detection in multi-temporal dual polarization Sentinel-1 data. International Geoscience and Remote Sensing Symposium (IGARSS) 2017-July, 3901–3908. https://doi.org/10.1109/IGARSS.2017.8127854

Nijhawan, R., Das, J., Raman, B., 2019. A hybrid of deep learning and hand-crafted features based approach for snow cover mapping. International Journal of Remote Sensing 40, 759–773. https://doi.org/10.1080/01431161.2018.1519277

Nolin, A.W., Payne, M.C., 2007. Classification of glacier zones in western Greenland using albedo and surface roughness from the Multi-angle Imaging SpectroRadiometer (MISR). Remote Sensing of Environment 107, 264–275. https://doi.org/https://doi.org/10.1016/j.rse.2006.11.004

Nuth, C., Kohler, J., König, M., von Deschwanden, A., Hagen, J.O., Kääb, A., Moholdt, G., Pettersson, R., 2013. Decadal changes from a multi-temporal glacier inventory of Svalbard. The Cryosphere 7, 1603–1621. https://doi.org/10.5194/tc-7-1603-2013

Østrem, G., 1975. ERTS data in glaciology—An effort to monitor glacier mass balance from satellite imagery. Journal of Glaciology 15, 403–415.

Pachauri, R.K., Allen, M.R., Barros, V.R., Broome, J., Cramer, W., Christ, R., Church, J.A., Clarke, L., Dahe, Q., Dasgupta, P., 2014. Climate change 2014: synthesis report. Contribution of Working Groups I, II and III to the fifth assessment report of the Intergovernmental Panel on Climate Change. Ipcc.

Partington, K.C., 1998. Discrimination of glacier facies using multi-temporal SAR data. Journal of Glaciology 44, 42–53. https://doi.org/DOI: 10.3189/S0022143000002331

Paterson, W.S.B., 1994. Physics of glaciers. Butterworth-Heinemann.

Patterson, J., Gibson, A., 2017. Deep learning: A practitioner's approach. " O'Reilly Media, Inc."

Paul, F., Barrand, N.E., Baumann, S., Berthier, E., Bolch, T., Casey, K., Frey, H., Joshi, S.P., Konovalov, V., le Bris, R., Mölg, N., Nosenko, G., Nuth, C., Pope, A., Racoviteanu, A., Rastner, P., Raup, B., Scharrer, K., Steffen, S., Winsvold, S., 2013. On the accuracy of glacier outlines derived from remote-sensing data. Annals of Glaciology 54, 171–182. https://doi.org/10.3189/2013AoG63A296

Paul, F, Barrand, N.E., Baumann, S., Berthier, E., Bolch, T., Casey, K., Frey, H., Joshi, S.P., Konovalov, V., le Bris, R., Mölg, N., Nosenko, G., Nuth, C., Pope, A., Racoviteanu, A., Rastner, P., Raup, B., Scharrer, K., Steffen, S., Winsvold, S., 2013. On the accuracy of glacier outlines derived from remote-sensing data. Annals of Glaciology 54, 171–182. https://doi.org/DOI: 10.3189/2013AoG63A296

Paul, F., Kääb, A., 2005. Perspectives on the production of a glacier inventory from multispectral satellite data in Arctic Canada: Cumberland Peninsula, Baffin Island. Annals of Glaciology 42, 59–66. https://doi.org/10.3189/172756405781813087

Pellikka, P., Rees, W.G., 2009. Remote sensing of glaciers: techniques for topographic, spatial and thematic mapping of glaciers. CRC press.

Persello, C., Stein, A., 2017. Deep Fully Convolutional Networks for the Detection of Informal Settlements in VHR Images. IEEE Geoscience and Remote Sensing Letters 14, 2325–2329. https://doi.org/10.1109/LGRS.2017.2763738

Pfeffer, W.T., Arendt, A.A., Bliss, A., Bolch, T., Cogley, J.G., Gardner, A.S., Hagen, J.-O., Hock, R., Kaser, G., Kienholz, C., Miles, E.S., Moholdt, G., Mölg, N., Paul, F., Radić, V., Rastner, P., Raup, B.H., Rich, J., Sharp, M.J., 2014. The Randolph Glacier Inventory: a globally complete inventory of glaciers. Journal of Glaciology 60, 537–552. https://doi.org/10.3189/2014JoG13J176

Pope, A., Rees, G., 2014a. Using in situ spectra to explore landsat classification of glacier surfaces. International Journal of Applied Earth Observation and Geoinformation 27, 42–52. https://doi.org/10.1016/j.jag.2013.08.007

Pope, A., Rees, W.G., 2014b. Impact of spatial, spectral, and radiometric properties of multispectral imagers on glacier surface classification. Remote Sensing of Environment 141, 1–13. https://doi.org/10.1016/j.rse.2013.08.028

Pope, A.J., 2013. Multispectral Classification and Reflectance of Glaciers: in situ data collection, satellite data algorithm development, and application in Iceland & Svalbard 146.

Pörtner, H.-O., Roberts, D.C., Masson-Delmotte, V., Zhai, P., Tignor, M., Poloczanska, E., Weyer, N.M., 2019. The ocean and cryosphere in a changing climate. IPCC Special Report on the Ocean and Cryosphere in a Changing Climate.

Rabatel, A., Sirguey, P., Drolon, V., Maisongrande, P., Arnaud, Y., Berthier, E., Davaze, L., Dedieu, J.P., Dumont, M., 2017a. Annual and seasonal glacier-wide surface mass balance quantified from changes in glacier surface state: A review on existing methods using optical satellite imagery. Remote Sensing 9. https://doi.org/10.3390/rs9050507

Rabatel, A., Sirguey, P., Drolon, V., Maisongrande, P., Arnaud, Y., Berthier, E., Davaze, L., Dedieu, J.P., Dumont, M., 2017b. Annual and seasonal glacier-wide surface mass balance quantified from changes in glacier surface state: A review on existing methods using optical satellite imagery. Remote Sensing 9. https://doi.org/10.3390/rs9050507

Racoviteanu, A., Williams, M.W., 2012. Decision tree and texture analysis for mapping debris-covered glaciers in the Kangchenjunga area, eastern Himalaya, Remote Sensing. https://doi.org/10.3390/rs4103078

Rau, F., Braun, M., Friedrich, M., Weber, F., Gobmann, H., 2000. Radar glacier zones and their boundries as indicators of glacier mass balance and climatic variability. Earsel eProceedings 317–327.

Raup, B., Racoviteanu, A., Khalsa, S.J.S., Helm, C., Armstrong, R., Arnaud, Y., 2007. The GLIMS geospatial glacier database: A new tool for studying glacier change. Global and Planetary Change 56, 101–110. https://doi.org/10.1016/j.gloplacha.2006.07.018

Riggs, G.A., Hall, D.K., Salomonson, V. v, 1994. A snow index for the Landsat thematic mapper and moderate resolution imaging spectroradiometer, in: Proceedings of IGARSS'94-1994 IEEE International Geoscience and Remote Sensing Symposium. IEEE, pp. 1942–1944.

Ronneberger, O., Fischer, P., Brox, T., 2015. U-Net: Convolutional Networks for Biomedical Image Segmentation. pp. 234–241. https://doi.org/10.1007/978-3-319-24574-4_28

Rusk, N., 2016. Deep learning. Nature Methods 13, 35. https://doi.org/10.1038/nmeth.3707

Saetrang, A.Chr., Wold, B., 1986. Results from the Radio Echo-Sounding on Parts of the Jostedalsbreen Ice Cap, Norway. Annals of Glaciology 8, 156–158. https://doi.org/DOI: 10.3189/S026030550000135X

Shi, J., Dozier, J., 1993. Measurements of snow- and glacier-covered areas with single-polarization SAR. Annals of Glaciology 17, 72–76. https://doi.org/10.3189/s0260305500012635

Shimamura, Y., Izumi, T., Matsuyama, H., 2006. Evaluation of a useful method to identify snow-covered areas under vegetation - Comparisons among a newly proposed snow index, normalized difference snow index, and visible reflectance. International Journal of Remote Sensing 27, 4867–4884. https://doi.org/10.1080/01431160600639693

Shukla, A., Ali, I., 2016. A hierarchical knowledge-based classification for glacier terrain mapping: A case study from Kolahoi Glacier, Kashmir Himalaya. Annals of Glaciology 57, 1–10. https://doi.org/10.3189/2016AoG71A046

Shukla, A., Yousuf, B., 2017. Evaluation of multisource data for glacier terrain mapping: a neural net approach. Geocarto International 32, 569–587. https://doi.org/10.1080/10106049.2016.1161078

Sibandze, P., Mhangara, P., Odindi, J., Kganyago, M., 2014. A comparison of Normalised Difference Snow Index (NDSI) and Normalised Difference Principal Component Snow Index (NDPCSI) techniques in distinguishing snow from related land cover types. South African Journal of Geomatics 3, 197. https://doi.org/10.4314/sajg.v3i2.6

Singh, S.K., Kulkarni, A. v., Chaudhary, B.S., 2010. Hyperspectral analysis of snow reflectance to understand the effects of contamination and grain size. Annals of Glaciology 51, 83–88. https://doi.org/10.3189/172756410791386535

Stocker, T., 2014. Climate change 2013: the physical science basis: Working Group I contribution to the Fifth assessment report of the Intergovernmental Panel on Climate Change. Cambridge university press.

Tran, N., Rémy, F., Feng, H., Féménias, P., 2008. Snow facies over ice sheets derived from envisat active and passive observations. IEEE Transactions on Geoscience and Remote Sensing 46, 3694–3708. https://doi.org/10.1109/TGRS.2008.2000818

Vikhamar-Schuler, D., Isaksen, K., Haugen, J.E., Tømmervik, H., Luks, B., Schuler, T.V., Bjerke, J.W., 2016. Changes in Winter Warming Events in the Nordic Arctic Region. Journal of Climate 29, 6223–6244. https://doi.org/10.1175/JCLI-D-15-0763.1

Wang, G., Liu, Y., Shen, H., Zhou, S., Liu, J., Sun, H., Tao, Y., 2021. Glacier Area Monitoring Based on Deep Learning and Multi-sources Data, in: Liu, Q., Liu, X., Shen, T., Qiu, X. (Eds.), The 10th International Conference on Computer Engineering and Networks. Springer Singapore, Singapore, pp. 409–418.

Williams, R.S., 1987. Satellite remote sensing of Vatnajökull, Iceland. Annals of Glaciology 9, 127–135.

Williams, R. S., Hall, D.K., Benson, C.S., 1991. Analysis of glacier facies using satellite techniques. Journal of Glaciology 37, 120–128. https://doi.org/10.1017/s0022143000042878

Williams, Richard S, Hall, D.K., Benson, C.S., 1991. Analysis of glacier facies using satellite techniques. Journal of Glaciology 37, 120–128. https://doi.org/DOI: 10.3189/S0022143000042878

Winsvold, S.H., Kääb, A., Nuth, C., Andreassen, L.M., van Pelt, W.J.J., Schellenberger, T., 2018. Using SAR satellite data time series for regional glacier mapping. The Cryosphere 12, 867–890.

WMO, United Nations Educational Scientific and Cultural organization, United Nations Environment Programme, International Council for Science, 2011. GCOS, 154. Systematic observation requirements for satellite-based data products for climate Supplemental details to the satellite-based component of the "Implementation Plan for the Global Observing System for Climate in Support of the UNFCCC (2010 Updat 139.

Xie, Z., Haritashya, U.K., Asari, V.K., Young, B.W., Bishop, M.P., Kargel, J.S., 2020. GlacierNet: A Deep-Learning Approach for Debris-Covered Glacier Mapping. IEEE Access 8, 83495–83510. https://doi.org/10.1109/ACCESS.2020.2991187

Xin, Y., Kong, L., Liu, Z., Chen, Y., Li, Y., Zhu, H., Gao, M., Hou, H., Wang, C., 2018. Machine Learning and Deep Learning Methods for Cybersecurity. IEEE Access 6, 35365–35381. https://doi.org/10.1109/ACCESS.2018.2836950

Yavaşli, D.D., Tucker, C.J., Melocik, K.A., 2015. Change in the glacier extent in Turkey during the Landsat Era. Remote Sensing of Environment 163, 32–41. https://doi.org/10.1016/j.rse.2015.03.002

Yokoya, N., Grohnfeldt, C., Chanussot, J., 2017. Hyperspectral and multispectral data fusion: A comparative review of the recent literature. IEEE Geoscience and Remote Sensing Magazine 5, 29–56. https://doi.org/10.1109/MGRS.2016.2637824

Yousuf, B., Shukla, A., Arora, M., Jasrotia, A., 2019. Glacier facies characterization using optical satellite data: Impacts of radiometric resolution, seasonality, and surface morphology. Progress in Physical Geography: Earth and Environment 43, 030913331984077. https://doi.org/10.1177/0309133319840770

Zhang, J., Jia, L., Menenti, M., Hu, G., 2019. Glacier facies mapping using a machine-learning algorithm: The Parlung Zangbo Basin case study, Remote Sensing. https://doi.org/10.3390/rs11040452

Zhang, Z., Liu, Q., Wang, Y., 2018. Road Extraction by Deep Residual U-Net. IEEE Geoscience and Remote Sensing Letters 15, 749–753. https://doi.org/10.1109/LGRS.2018.2802944

Zhong, Z., Li, J., Cui, W., Jiang, H., 2016. Fully convolutional networks for building and road extraction: Preliminary results, in: 2016 IEEE International Geoscience and Remote Sensing Symposium (IGARSS). pp. 1591–1594. https://doi.org/10.1109/IGARSS.2016.7729406

10 APPENDIXES

10.1 Appendix -1

The Sentinel-1 C-band SAR instruments operate in single (HH or VV) and dual polarisation (HH+HV or VV+VH), with one transmit chain (switchable to H or V) and two parallel receive chains for H and V polarisation. The information about the copernicus Sentinel-1 programme is presented in image below.

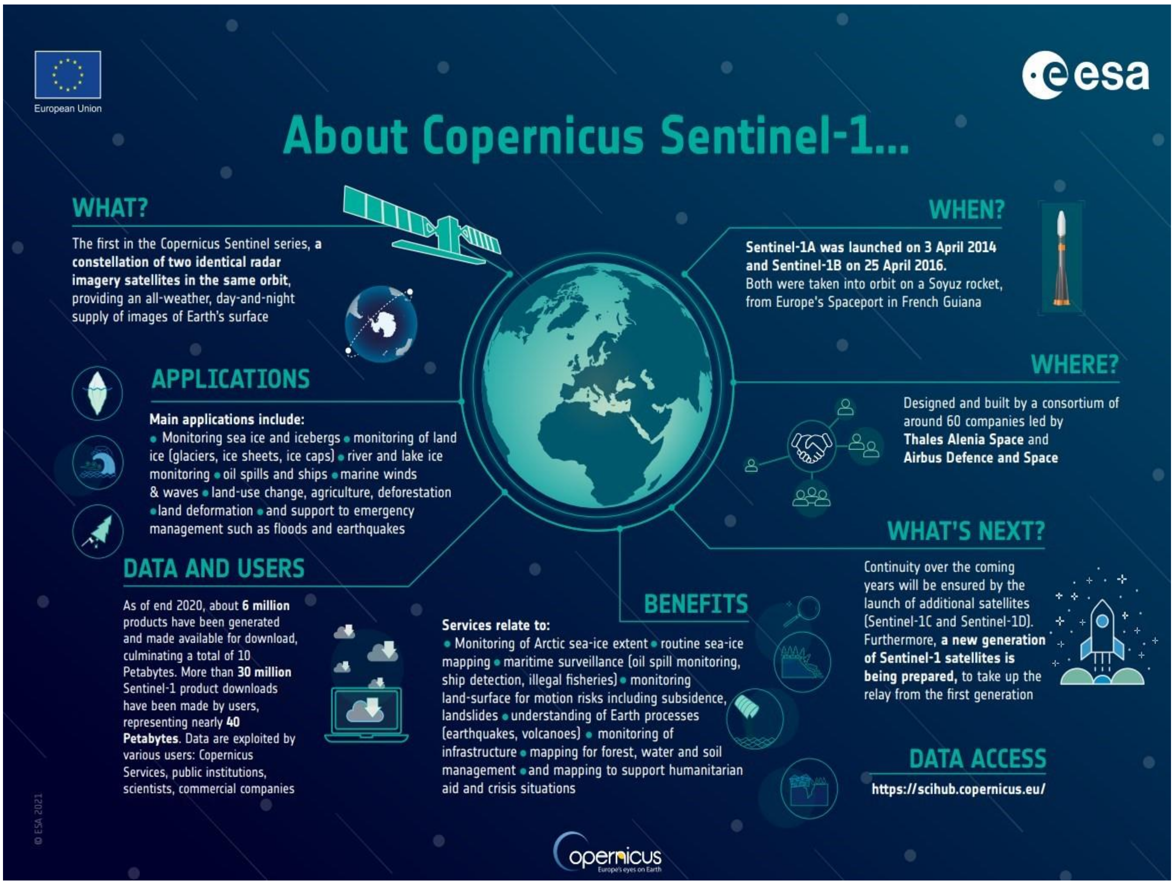

Figure 10.1: The overview of Sentinel-1 mission (Source: https://sentinel.esa.int/web/sentinel/missions/sentinel-1)

Table 10.1: Specification of Sentinel-1 level-1 product

Accusition Mode	Product type	Resolution Class	Spatial Resolution rg x az (m)	Pixel spacing rg x az (m)	Number of looks rg x az (m)
Stripmap (SM)	Single Look Complex (SLC)		1.7x4.3 m to 3.6x4.9 m	1.5x3.6 m to 3.1x4.1 m	1 x1
	Ground Range Detected (GRD)	Full Resolution (FR)	9 x 9	3.5 x 3.5	2 x 2
		High Resolution (HR)	23 x 23	10 x 10	6 x 6
		Medium Resolution (MR)	84 x 84	40 x 40	22 x 22
Interferometric Wide (IW)	Single Look Complex (SLC)		2.7x22 m to 3.5x22 m	2.3 x 14.1	1 x 1
	Ground Range Detected (GRD)	High Resolution (HR)	20 x 22	10 x 10	5 x 1
		Medium Resolution (MR)	88 x 87	40 x 40	22 x 5
Extra-Wide swath (EW)	Single Look Complex (SLC)		7.9x43 m to 15x43 m		1 x 1
	Ground Range Detected (GRD)	High Resolution (HR)		25 x 25	3 x 1
		Medium Resolution (MR)		40 x 40	6 x 2
Wave (WV)	Single Look Complex (SLC)		2.0x4.8 m and 3.1x4.8 m	1.7x4.1m and 2.7x4.1m	1 x 1
	Ground Range Detected (GRD)	Medium Resolution (MR)	52 x 51	25 x 25	13 x 13

10.2 Appendix -2

The information about the Sentinel-2 satellite

The S2 mission is of a twin-satellite programme with high revisit frequency, and high-resolution image which fulfill the goals of Copernicus programmes. As per mission guide the data from this mission can be mainly utilized for services such as:

- Land monitoring
- Emergency management
- Security
- Climate change, etc.

Table 10.2: Spectral bands for the SENTINEL-2 sensors (S2a & S2b)

	S2A		**S2B**		
Band Number	**Central wavelength (nm)**	**Bandwidth (nm)**	**Central wavelength (nm)**	**Bandwidth (nm)**	**Spatial resolution (m)**
1	442.7	21	442.3	21	60
2	492.4	66	492.1	66	10
3	559.8	36	559	36	10
4	664.6	31	665	31	10
5	704.1	15	703.8	16	20
6	740.5	15	739.1	15	20
7	782.8	20	779.7	20	20
8	832.8	106	833	106	10
8a	864.7	21	864	22	20
9	945.1	20	943.2	21	60
10	1373.5	31	1376.9	30	60
11	1613.7	91	1610.4	94	20
12	2202.4	175	2185.7	185	20